



High efficiency phototransducers based on a novel vertical epitaxial heterostructure architecture (VEHSA) with thin p/n junctions

Mark York, Simon Fafard

► To cite this version:

Mark York, Simon Fafard. High efficiency phototransducers based on a novel vertical epitaxial heterostructure architecture (VEHSA) with thin p/n junctions. *Journal of Physics D: Applied Physics*, 2017, 50 (17), 10.1088/1361-6463/aa60a6 . hal-01914380

HAL Id: hal-01914380

<https://hal.science/hal-01914380>

Submitted on 29 Nov 2018

HAL is a multi-disciplinary open access archive for the deposit and dissemination of scientific research documents, whether they are published or not. The documents may come from teaching and research institutions in France or abroad, or from public or private research centers.

L'archive ouverte pluridisciplinaire **HAL**, est destinée au dépôt et à la diffusion de documents scientifiques de niveau recherche, publiés ou non, émanant des établissements d'enseignement et de recherche français ou étrangers, des laboratoires publics ou privés.

Topical Review

High efficiency phototransducers based on a novel vertical epitaxial heterostructure architecture (VEHSA) with thin p/n junctions

Mark C A York¹ and Simon Fafard^{1,2}

¹ Laboratoire Nanotechnologies Nanosystèmes (LN2)—CNRS UMI-3463, Institut Interdisciplinaire d'Innovation Technologique (3IT), Université de Sherbrooke, Sherbrooke, QC, J1K OA5, Canada

² Azastra Opto Inc., Ottawa, Ontario, K1W 1G3, Canada

E-mail: simon.fafard@usherbrooke.ca

Received 30 April 2016, revised 6 February 2017

Accepted for publication 15 February 2017

Published 28 March 2017



Abstract

This review outlines a series of developments in the design, modelling and growth of multi-junction laser power converters, including several observations of multi-junction GaAs monolithic vertical epitaxial heterostructure architecture devices with astonishing monochromatic optical to electrical conversion efficiencies in the 65–70% range. Experimental data is presented for devices ranging from single up to 20 p/n junctions, generally exhibiting weak dependence on source detuning which serves as evidence for strong photon recycling effects in these devices. Considerations for further design optimizations are discussed in detail, as well as the future direction of this research including the growth of devices with up to 100 subcells.

Keywords: heterostructures, photovoltaics, p/n junctions, phototransducer, VEHSA, III–V, epitaxy

(Some figures may appear in colour only in the online journal)

1. Introduction

1.1. Motivation and applications

There has been significant progress in recent years in the development of laser power converters (LPC) [1–3] reflecting the growing demand for applications of power-over-fibre and systems requiring photonic energy converts (PECs). Any system which is reliant upon electrical shielding can benefit from advancements in this field, examples being found in medical [4] contexts and high-voltage [5] settings. With power-over-fibre, energy is transmitted at optical frequencies, originating from a monochromatic source and travelling via fibre optic

cables or through free space. The conversion back to electricity makes use of specialized PECs, essentially III–V photovoltaic cells designed to operate at a single wavelength and often high source intensities.

The development of PECs has accelerated in the past three years with the breakthrough implementation of the novel Vertical Epitaxial HeteroStructure Architecture (VEHSA design). Related studies have extended our understanding in this important field, including the experimental demonstration of photon coupling effects in devices with ultra-thin p/n junctions. Specifically, that photon coupling beneficially impacts the optical properties of such high-efficiency devices.

The VEHSA heterostructure design [6–12] is at the basis of unprecedented device performance and will surely have far reaching implications for various fields. These recent studies reveal the unique properties of nanoscale III–V semiconductor junctions which are at work in GaAs-based heterostructures



Original content from this work may be used under the terms of the [Creative Commons Attribution 3.0 licence](https://creativecommons.org/licenses/by/3.0/). Any further distribution of this work must maintain attribution to the author(s) and the title of the work, journal citation and DOI.

having such thin p/n junctions. Results are also providing key insight into important fields covering solar, optoelectronics, biomedical, information and communication technologies, sensors, and microelectronics applications.

It should be expected that the research, development, and commercialization for this new class of optical to electrical converting heterostructures and devices will continue to grow significantly in the near future. There has already been an increased interest for ultra-thin photovoltaic devices recently in the literature. The higher optical to electrical conversion efficiency will further generate important solutions enabling various applications for utilities and telecommunication (safe sensing and monitoring), for medical (safe and efficient neuro-stimulations to control various pathologies, and enabling durable life-supporting or life-enhancing implants), aerospace or power electronics applications (providing sustainability, safety, or entertainment features). The insight provided by the research in this field should also increase versatility in the design of a wide range of optoelectronic devices and push the limits in applied physics.

1.2. Review of background and previous research in the area

As of 2008 efficiencies of 53.4% were reported for GaAs LPC devices [2], at a time when hetero multi-junction solar cells were only reaching slightly above 40% [13]. Prior to writing this review, the present authors have reported conversion efficiencies of 69.5% for a functionally similar device [6] (contrasted with the more modest gains in multi-junction solar cells over the same period which have reached 46% [14]). It is interesting to note that [2] estimates the highest attainable efficiency for a GaAs LPC to be just under 65%, when factoring in both losses due to sheet resistance, recombination, and manufacturing as well as the theoretical upper bound for the performance of these devices—a monochromatic analogue of the Shockley Queisser (SQ) limit. Note also that while lab demonstrations have been shown with ~50% efficiencies, the range in production is more like 30% to 40% due to additional resistive and optical losses commonly obtained while implementing the planar multi-junction geometry. This result prompts a reconsideration of our intuition for the processes which traditionally limit device performance.

Neither the SQ nor Carnot limit apply to monochromatic LPCs, which can be understood in simple terms as a consequence of source illumination originating from a system which is not in thermal equilibrium. For these devices, the limit of 100% conversion is asymptotically approached for increasing source intensity. In practice the efficiency is mainly limited by the magnitude of the output voltage (e.g. open circuit voltage or V_{oc}), and the fill factor (FF) coefficient of the current–voltage $I(V)$ curve of the device, while the quantum efficiency (EQE) and the short circuit currents (I_{sc}) can approach very close to their optimum values. Moreover, upper bounds on solar cell efficiency in theoretical scenarios involving a large or infinite number of junctions (effectively PV devices with more than three junctions) are fundamentally unattainable in the near future due to semiconductor lattice mismatch issues. Multi-junction LPCs, however, do not suffer

from this problem, as all subcells must have the same band gap and hence can be fabricated from the same semiconductor [7]. Thus, it is practical to consider devices with a large number of p/n junctions, and experimental results in this text are presented for devices with up to 20 junctions stacked in a vertical arrangement [8].

1.3. Overview of the VEHS design and growth details

N-junction (PTN) vertical epitaxial heterostructure architecture (VEHSA) devices have been grown by metal organic chemical vapour deposition (MOCVD) using an Aixtron 2600 multi-wafer reactor. A schematic illustration of such a device (in this case PT20, i.e. 20 junctions) is shown in figure 1. The range of N for which we have reported experimental data goes from 1 (single p/n junctions) up to 20, though currently our research is focused on expanding this number further yet, with PT100 devices considered potentially viable [8].

Basic features include an $n \sim 2 \times 10^{18} \text{ cm}^{-3}$ n-type $1 \mu\text{m}$ InGaP window and buffer layers, AlGaAs (Al molar fraction not exceeding 30%) n++/p++ tunnel junctions and GaAs p/n junctions. Devices are optimized for target wavelengths in the range 750–875 nm—over this range the InGaP and AlGaAs layers are transparent to the probe light. A thick top window layer is implemented as it assists with carrier extraction at high optical input powers. Junction thicknesses are established by current-matching between adjacent junctions for a specified target wavelength—for a set absorption coefficient α and total GaAs thickness t individual layer thicknesses t_i can be calculated analytically. Further care must be taken in any limit where junctions become sufficiently thin as to require a treatment of quantum effects.

VEHSA structures have been implemented successfully with various types of tunnel junctions [7]. Key desired features of the tunnel junctions are high transparency to the optical input and high peak current capability. Various alloy compositions and doping profiles have been realised successfully. A prevalent choice, frequently used also for concentrated photovoltaic (CPV) applications, is the n++ InGaP/p++ AlGaAs pair. Te or Se are typically used for doping n-type above $1 \times 10^{19} \text{ cm}^{-3}$ and C or other p dopants are typically used for doping p-type above $1 \times 10^{19} \text{ cm}^{-3}$. While the above tunnel junction combination has demonstrated good performance for CPV applications, current densities with power converting devices can be significantly higher than for CPV, reaching above 1 kW cm^{-2} in some cases. It has also been shown recently that the n++ AlGaAs/p++ AlGaAs pair can support higher peak current by selecting an Al composition between 10% and 30% and dopants and doping levels comparable to the n++ InGaP/p++ AlGaAs tunnel junctions. The AlGaAs pair has therefore been used for the majority of the results presented here. Regardless of the choice of tunnel junction alloy combination, the resulting band diagram features an effective photovoltage step up conversion as illustrated in figure 1(b) [15].

GaAs junctions contain n-type emitters and p-type bases. Though the combined thickness of each p/n junction

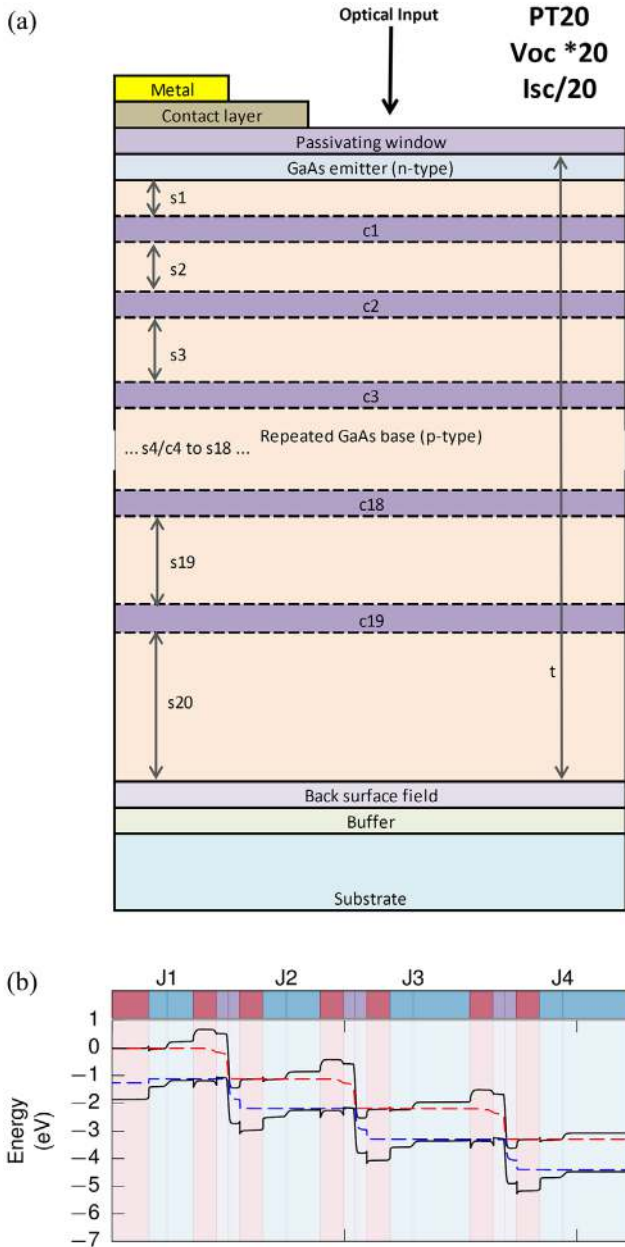


Figure 1. (a) Schematic depiction of the individual layers in a 20 junction (PT20) VEHS (n-type emitter only shown explicitly for the topmost subcell). (b) Example of the calculated energy band diagram of the upper most junctions (J1, J2, J3, etc) of a VEHS structure. Adapted from [15], with the permission of AIP Publishing.

is constrained, the proportion of emitter and base are arbitrary. When specifying these quantities we adopt the following strategy: for junctions with thickness $t_i < 200$ nm, t_i is evenly split between the base and emitter. However, whenever t_i exceeds 200 nm, the emitter is fixed at 100 nm with the base making up the rest. Base and emitter dopings are of the order $n \sim 10^{18} \text{ cm}^{-3}$, with slight adjustments made with junction thickness (thinner subcells are in general more heavily doped than thicker ones). Simulations carried out in the past have shown negligible variations in conversion efficiency for adjustments over the range $1 \times 10^{18} \text{ cm}^{-3}$ – $2 \times 10^{18} \text{ cm}^{-3}$. Over this range gains in V_{oc} are offset by reductions in carrier lifetimes, therefore it is difficult to make a tangible impact on

PV efficiency by adjusting these quantities, and values outside of this range would likely yield a decrease in efficiency either via diminished V_{oc} or minority carrier lifetime.

Electrodes are patterned via contact mask lithography, with gridlines approximately $5 \mu\text{m}$ wide. Layouts of the aperture are shown in figure 2—a D-like (dense) pattern is used in production though we have conducted experiments on E (intermediate) and F (sparse) patterned devices. The aperture diameter of physical devices varies, though for modelling purposes we adopt a standard of $2240 \mu\text{m}$. It should be noted that the cell size and the grid designs of figure 2 have been used a lot experimentally and for modelling purposes, but comparable results have been obtained with various geometries, including smaller and bigger cells. When designing a VEHS, it is important to consider that there will be some variability in the layer thicknesses of physical devices, and furthermore, that this variability can be random. Fortunately, slight current mismatches between adjacent junctions are compensated for by luminescent coupling, and in turn, these devices serve as a good proxy for studying photon recycling [16].

1.4. Comparison between the vertical and horizontal architectures

Optimization of photovoltaic conversion efficiency occurs when the absorption of incoming photons and electron-hole extraction are maximized at the same time. This challenge can therefore be separated into the simultaneous optimization of the parameters I_{sc} , FF , and V_{oc} . Achieving V_{oc} close to the theoretical limit is therefore crucial for performance—it has recently been demonstrated experimentally that nanoscale layers can achieve a larger Fermi level splitting, and thus increased V_{oc} [17].

High photovoltages and conversion efficiencies have been reported with GaAs planar or vertical arrangements, in particular at high optical intensities [2, 3, 12, 18–39]. However, a vertical architecture is particularly effective, as record-high photovoltages and unprecedented monochromatic conversion efficiencies have been achieved with the VEHS design [6–12]. The VEHS monolithic design allows one to construct n/p junction devices with minimal shunting and series resistance. Series resistances of only a few milliohms are readily achieved in this configuration, permitting high FF values in operation. In turn, VEHS devices can be operated with an optical input generated from a laser diode with several watts of incident power.

The I_{sc} value of these photovoltaic devices can simply be determined by the responsivity of the heterostructure (R , in A W^{-1}), with $I_{sc} = R \times P_{in}$, where P_{in} is the input power of the optical source. Furthermore, the responsivity R is given by $QE \times \lambda/hc = QE/1239.85 \times \lambda$ when λ (the input wavelength) is in nm, h and c are the Planck and the speed of light constants respectively, QE is the quantum efficiency (for example the external quantum efficiency, i.e. EQE), and R in A W^{-1} . It has also been demonstrated experimentally that strong photon coupling effects [15, 16, 40–44] are making important contributions to the responsivity of the VEHS devices. The latter is also beneficial in vertical structures for obtaining improved I_{sc}

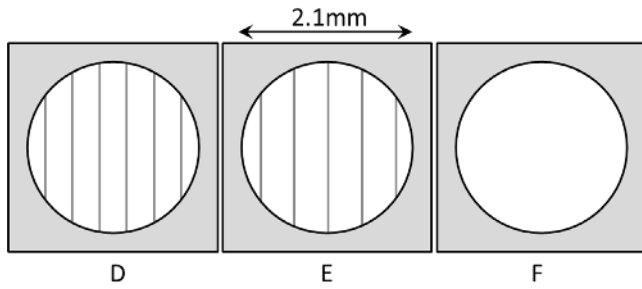


Figure 2. Various gridline patterns. The ‘D’ pattern is observed to be sufficiently dense as to not hinder carrier extraction, while the ‘F’ pattern is sparse (resulting in reduced fill factors). Spacings are $325\ \mu\text{m}$ and $425\ \mu\text{m}$ for the D and E patterns respectively, with approximately $5\ \mu\text{m}$ thick gridlines. [7] John Wiley & Sons. © 2015 John Wiley & Sons, Ltd.

values, particularly when the optical input is detuned from the peak of the spectral response. This effect is especially advantageous for the VEHSAs given that all the subcells have the same absorption characteristics [6–8]. At high input intensities, these photon recycling effects allow for maintaining a high responsivity over a broad wavelength range.

An example directly comparing the vertical and horizontal architectures is shown in figure 3. The improved V_{oc} obtained with the thin n/p junctions is readily observed in figure 3 by comparing the V_{oc} results of a 6-junction device, designed with the planar architecture made of standard n/p junctions, to the PT6 device (VEHSA design with 6 thin vertical n/p junctions). A gain of $\sim 92\ \text{mV}$ per n/p junction is observed. By comparison to the planar device, a similar gain in V_{oc} is obtained with both the PT6 and the PT12 devices.

This data also demonstrates that the responsivity values of the PT6 and the PT12 devices are twice that of the planar photovoltaic device. For example, it has been shown for the VEHSAs that EQE values of up to 94% can be achieved at the peak of the spectral response [8]. As mentioned above, the responsivity is directly proportional to the value of the incident wavelength and to the EQE. Therefore, optimal efficiency will be obtained at longer wavelengths near the bandgap and when the EQE is approaching unity. Figure 3 also shows the theoretical maximum responsivity for the corresponding EQE values for the wavelengths 823 nm (optical input used for PT6) and 850 nm (optical input used for PT12). From this it is clear that the maximum performance for the associated QE values has been fully achieved with the VEHSAs.

Figure 3 reveals that the planar device displays significant shunting issues (slope in the horizontal section of the $I(V)$ curve) and series resistance issues (slope in the vertical section of the $I(V)$ curve). Since the VEHSAs do not exhibit this behaviour, they can readily convert in excess of 3 W of output power with an efficiency over 60% as observed in figure 3.

1.5. Simulations, overview of recent progresses, and status in the field

Recent progress with VEHSAs has demonstrated the following performance attributes:

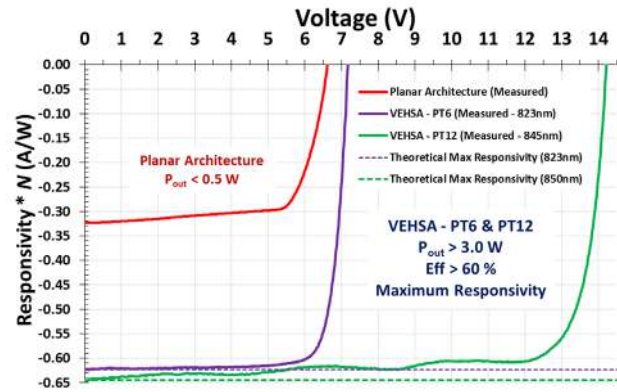


Figure 3. Responsivity curves measured at $25\ ^\circ\text{C}$ for VEHSA devices having 6 (PT6) and 12 (PT12) thin n/p junctions. The VEHSA heterostructures are near current-matched for the wavelengths indicated in the legend. The theoretical maximum responsivity is also shown for the wavelengths of 823 nm and 850 nm for EQE values of 94% and 93% respectively. Data for a planar device with 6 junctions configured in a parquet geometry is also shown for comparison. [45] John Wiley & Sons© 2016 WILEY-VCH Verlag GmbH & Co. KGaA, Weinheim.

- The highest optical to electrical efficiency ever achieved [6, 8].
- The highest output powers ever reported for a high-efficiency monolithic PV cell with 5.87 W of converted output [45].
- The highest efficiencies ever reported for any types of optical to electrical power conversion devices simultaneously combining high photovoltage and output powers ($>5\ \text{W}$ at $>7\ \text{V}$ with $>60\%$ efficiency and $>3\ \text{W}$ at $>14\ \text{V}$ with $>60\%$ efficiency) [45].
- Unique experimental evidence of the significant impact of photon recycling in these photovoltaic devices [45].
- The highest efficiency ever reported of 61.8% with a significantly detuned optical input [45].

Given the present status of PECs in the 810–850 nm range, further optimization could also be obtained by designing the VEHSAs for operation at longer wavelengths to reach higher values of responsivity (i.e. minimizing thermalization losses) and by further increasing EQE values closer to 100%. In the following section we review some of the simulations performed to better understand the properties of these devices.

1.5.1. Challenges in constructing an effective model. We frequently turn to numerical models to gain valuable insight into the observed trends in performance of the VEHSAs. Though idealized in many regards, a TCAD model allows us to assess the performance impact of design variables otherwise inaccessible experimentally (e.g. minority carrier lifetimes of a single layer). However, there are certain configurations where we expect modelled data to deviate from experiment.

Accurately simulating a PTN heterostructure (figure 1) in TCAD is not a simple task, various setbacks are encountered due to numerical complexity and poor convergence. From a strictly model construction standpoint, a PTN device is described by a large set of variables:

- (i) layer thicknesses,
- (ii) emitter and base dopings in each junction,
- (iii) minority carrier lifetimes for each alloy,
- (iv) carrier mobilities for each alloy,
- (v) incident beam intensities and profile,
- (vi) tunnel junction molar fractions, dopings, thicknesses etc,
- (vii) radiative recombination rates and photon recycling,
- (viii) band gap narrowing,
- (ix) incident wavelength and material absorption coefficients.

Some of the material parameters used here are summarized in tables 1, 2 and 3. The list above it not exhaustive, though, many of these variables are either constrained or nominally pre-determined in some fashion, leaving a smaller subset of truly *free* parameters (these *free* parameters are either those design variables which if fortuitously adjusted, could yield higher yet PV conversion efficiencies, or intrinsic material parameters not well constrained by experiment). To clarify, (i) are fixed as a requirement of current-matching, and should closely coincide with those layer thicknesses used in fabrication. (iii) can be found in the literature, with some scatter in the data [37, 46–48]. (iv) are fairly well constrained for the materials being used [49]. If we are able to assume that the tunnel junctions are sufficiently well approximated as zero-loss, then (vi) become irrelevant as it is unnecessary to model the actual tunnelling process [50]. (ix) go hand in hand with (i) and a generally constrained by design and experiment (see table 2). Given this, what remain as *free* parameters are (ii), (v), (vii), (viii) and to a lesser extent (iii).

Emitter and base dopings are tuned to yield optimal V_{oc} , though as mentioned in section 1 there is in fact not a lot of freedom here, as values too low result in deteriorating V_{oc} while values too high lead to short carrier lifetimes. For our purposes, the optimum range is typically around 10^{18} cm^{-3} . Minority carrier (specifically SRH) lifetimes for GaAs are stated in the literature, with expected values of the order $\sim 100 \text{ ns}$ [48] for bulk GaAs; however, these values can be affected by the quality of the growth, nor are they constant with injection level [46]. We adopt conservative estimates for these lifetimes via calibration, and assess the strength of the associated dependence of modelled data, which we generally find to be weak. In our case, the values implemented numerically were set via calibration to experimental data for single junction devices grown using the same set-up as for the multi-junctions [9–11]. Band gap narrowing presents a challenge to accurately modelling the V_{oc} . Since the exact values are not well constrained experimentally [51] (or in fact conflicted, noting an approximately 80 meV difference in the narrowing for n-GaAs at 10^{18} cm^{-3} doping between [51] and [52]). As with the SRH lifetimes, we consider the degree of variation in modelled data in both limits.

Photon recycling presents a major challenge, as these effects are difficult to model explicitly without introducing a high level of numerical complexity. In these devices photon recycling allows for emissions followed by reabsorptions in separate junctions. Moreover, photon recycling mitigates detuning, since an excess of radiative recombinations in over-producing junctions will transfer current to adjacent subcells.

Table 1. Material parameters (SRH lifetimes, carrier mobilities and radiative recombination rates) used in simulation.

Parameter	Value
τ_n	10 ns @ $n = 10^{18} \text{ cm}^{-3}$
τ_p	35 ns @ $n = 10^{18} \text{ cm}^{-3}$
μ_n^{GaAs}	$2600 \text{ cm}^2 \text{ Vs}^{-1}$ @ $n = 10^{18} \text{ cm}^{-3}$
μ_p^{GaAs}	$170 \text{ cm}^2 \text{ Vs}^{-1}$ @ $n = 10^{18} \text{ cm}^{-3}$
μ_n^{InGaP}	$550 \text{ cm}^2 \text{ Vs}^{-1}$ @ $n = 2 \times 10^{18} \text{ cm}^{-3}$
μ_p^{InGaP}	$30 \text{ cm}^2 \text{ Vs}^{-1}$ @ $n = 2 \times 10^{18} \text{ cm}^{-3}$
B	$1.6 \times 10^{-10} \text{ cm}^3 \text{ s}^{-1}$

Table 2. Values of α at several wavelengths of interest. In the rightmost column we list the devices modelled in each case at these wavelengths.

Wavelength (nm)	Value (cm^{-1})	Devices
825	13 500	6J
830	12 837	1J, 5J, 12J
839	11 500	5J, 12J
850	9410	5J, 8J, 12J
860	7414	5J, 12J

Barring a brute force simulation, there are various strategies we can adopt to approximate and infer the relative size of these effects. As a start, we can eliminate radiative recombinations entirely, allowing us to estimate the maximum possible enhancement in efficiency attributable (observed to be typically 1–2% when current matched). Such an approach is viable at design wavelengths, since in this case, photon recycling at best reduces the effective radiative recombination rate, hence the maximum enhancement achievable is that for $B = 0$. We can then take this a bit further and adjust the radiative recombination rate in each junction as a function of junction size ($B \rightarrow B(1 - \gamma_i)$) with a junction dependent suppression factor γ_i —this would accommodate emissions and reabsorptions which occur in the same junction, but not those neighbouring. Such an approach is a better approximation in current matched conditions; however both of these approximations would fail whenever the source wavelength is detuned from the design wavelength. In these cases we observe the largest discrepancy between measured and modelled data, though a more rigorous treatment of photon recycling has been considered elsewhere [16].

(v) Presents a lesser challenge than (vii). In this case, the range of intensities being modelled coincides with the range experimentally, so the open problem lies with the exact shape of the source beam profile. It is safe to assume that experimental fibre optic sources are not uniform in intensity over the fibre's acceptance cone, nor should the beam be overly narrow as to introduce unnaturally large current densities in the device. Fortunately, for fixed source current the dependence of beam intensity is fairly weak for any devices with dense gridline patterns, which can be said of all devices used in production.

Table 3. Eff (%) versus SRH lifetimes for the reference PT12 model.

τ_{n0} / τ_{p0} (ns)	1 ns	10 ns	100 ns
1	53.2	57.3	59.3
10	56.3	61.1	63.7
100	58.1	61.9	64.1

1.5.2. Details of the model and various sanity checks. Any simulated data that is presented in this review was obtained with Silvaco Atlas 5.19.20.R using a 2D axisymmetric approximation of the heterostructure, unless otherwise noted. A fully 3D model is not needed, since the only non-axisymmetric feature of the physical devices is the gridline pattern, and we only consider the extreme cases (a) where there are no gridlines (sparse F-pattern) and (b) where carrier extraction is efficient (dense D-pattern). That is, we are not interested in any fringe behaviour associated with the gridlines.

From the simulations we extract V_{oc} , I_{sc} and efficiency measurements while varying the free parameters. Furthermore, at times we consider the impact of non-tunable parameters (e.g. band gap narrowing in GaAs) to assess the robustness of the simulations.

SRH and radiative recombination are the dominant mechanisms in these devices, and we adjust the SRH lifetimes τ_n and τ_p for donor/acceptor concentration ρ via the simple power-law [47]

$$\tau_{n(p)}(\rho) = \tau_{n(p)0} \left(\frac{\rho}{10^{18} \text{ cm}^{-3}} \right). \quad (1)$$

This expression omits the plateau in τ at low dopings, though this is of no concern as all GaAs layers are doped.

To address the impact of non-tunable parameters, we will consider a reference 12 junction (4200 nm total GaAs thickness) heterostructure illuminated by an 8 W cm^{-2} source over a radius of $1033 \mu\text{m}$ (current-matched at 850 nm.) As a benchmark, we adjust τ_{n0} and τ_{p0} over the range 1 ns–100 ns, contrasting between (a) models with and without n-type GaAs BGN (table 4), (b) sources of varying diameter at constant input power P_{in} (table 5) and (c) models with and without radiative recombinations (table 6).

These numbers serve as a measure of the uncertainty in modelled efficiencies associated with poor constraints in these parameters. In summary, D-patterned devices under current matched conditions exhibit <1% scatter in efficiency due to radiative recombinations and source illumination acceptance angle, and as such, we rarely study adjustments to these parameters on a model-by-model basis.

Potential scatter due to SRH lifetimes (varied over two orders of magnitude) is on par with that due to nGaAs band gap narrowing—in these case we should simply make note that the associated errors are of the order a few %.

As a final remark, as the physical devices are tuned to various wavelengths, not all heterostructures are modelled at 850 nm. For reference, in table 2 we list the wavelengths studied numerically, as well as the associated PTN devices.

Table 4. Eff (%) versus SRH lifetimes for the reference PT12 model without n-type band gap narrowing.

τ_{n0} / τ_{p0} (ns)	1 ns	10 ns	100 ns
1	57.4	59.9	61.2
10	63.4	66.2	67.8
100	65.9	68.6	69.6

Table 5. Eff (%) versus SRH lifetimes for the reference PT12 model with an $I = 26 \text{ W cm}^{-2}$, $R = 572 \mu\text{m}$ source.

τ_{n0} / τ_{p0} (ns)	1 ns	10 ns	100 ns
1	53.3	57.5	59.5
10	56.4	61.3	63.8
100	58.2	62.0	64.2

Table 6. Eff (%) versus SRH lifetimes for the reference PT12 model with no radiative recombination (i.e. setting $B = 0$.)

τ_{n0} / τ_{p0} (ns)	1 ns	10 ns	100 ns
1	53.4	57.9	61.0
10	56.4	61.6	66.0
100	58.3	62.5	

Subtle variations in efficiency due to the thermalization losses at shorter wavelengths tends to add further scatter to the data.

1.5.3. Single junctions. The study and simulation of single junction devices serves as a good platform for calibrating model parameters. For our purposes single junction devices of thicknesses ranging from roughly $\sim 200 \text{ nm}$ to $\sim 2500 \text{ nm}$ were grown under similar conditions as the PTNs (further details are available in [10, 11].) Due to the simplicity of these devices, it is possible to achieve fairly tight agreement between modelled and experimental data, as shown in figure 4. For V_{oc} as shown, this agreement is typically at the level of 5mV to 10mV (note that as the thickness increases in figure 4, the base doping slightly decreases, resulting in the bent shape of the trend).

From figure 5 we observe that F-pattern devices typically exhibit reduced fill factor, though not apparent in thin devices when the current density is proportionately lower (likewise, F-pattern thin devices at very high source intensities also exhibit reduced fill factor). We can further analyze this behaviour by examining the electric fields inside the device, as shown in figure 6. One feature worthy of note is the formation of a characteristic depression or ‘void’ in E-field strength towards the centre of the device which only manifests itself whenever fill factors are low.

We can assess the impact of source radius on model output by measuring fill factor at fixed source power with narrowing beam radius (and hence increasing flux density). Results are shown in figure 5—though the F-patterned devices appear to be strongly affected by this, the D-pattern (production) devices are virtually insensitive to the beam profile except in the limit of a very narrow beam, confirming that a rigorous treatment

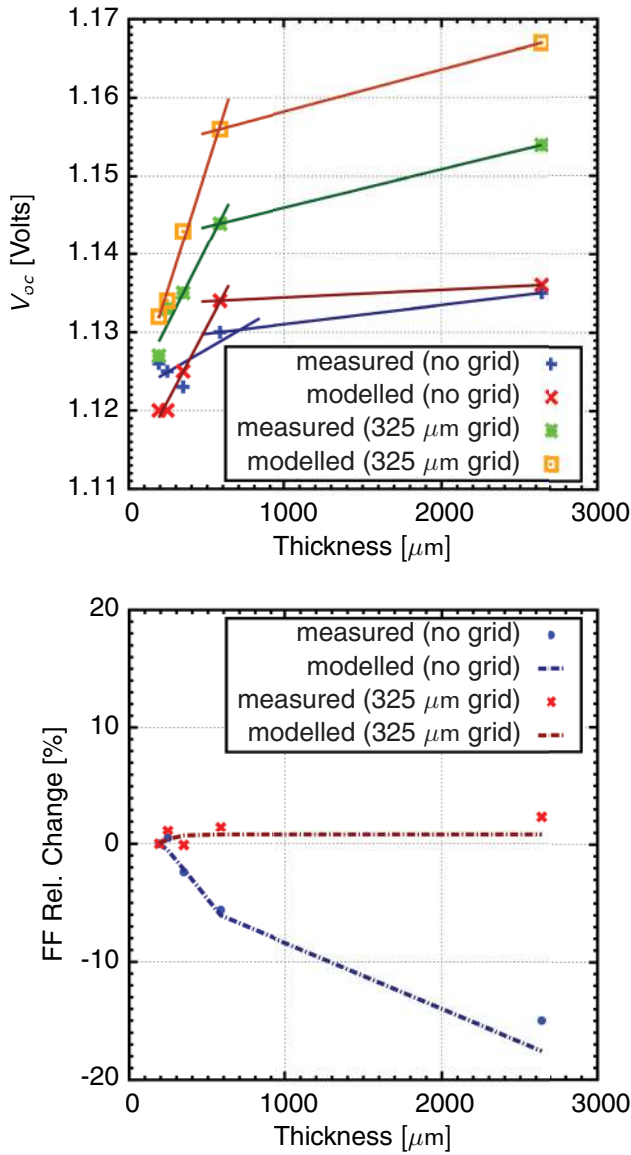


Figure 4. (Top panel) Comparison between simulated and measured V_{oc} for single junction devices of varying thicknesses. (Bottom panel) Graph illustrating the relative degradation in fill factor for F-patterned devices. Adapted with permission from [10, 11].

of source beam profile is unnecessary except when the beam is relatively narrow (a limit not studied experimentally).

1.5.4. Multiple junctions. Examples of modelled results are shown for multiple junctions in figures 7 and 8. Agreement between modelled and experimental results for PTN devices with $N \geq 5$ can be quite good under common operating conditions, as evidenced by figure 7. Deviations from exact agreement stem in a large part from difficulty in obtaining an exact match for V_{oc} due to BGN. Modelled I_{sc} values conversely are often nearly exact, as are fill factors for D-patterned devices.

Somewhat related to the challenges associated with simulating current-mismatched conditions, $I(V)$ curves do not exhibit the characteristic undulations of experimental $I(V)$ curves (barely apparent in figure 7—these are explained in more detail later in the text.) Model heterostructures always

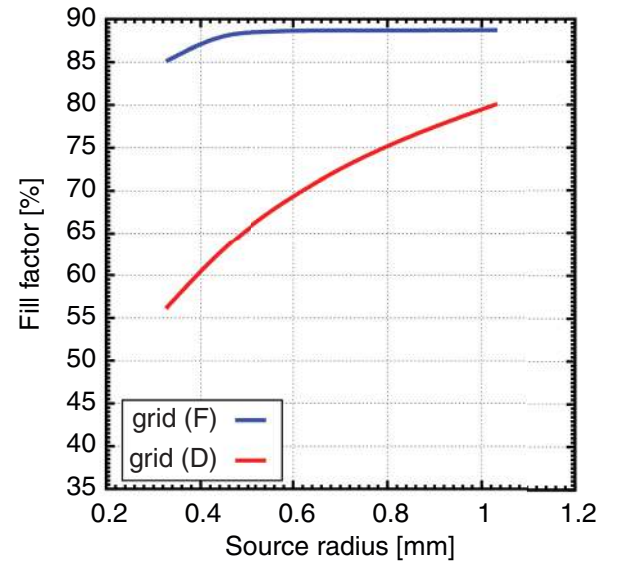


Figure 5. Fill factor versus beam radius at fixed source current, comparing between single junction devices with sparse and dense gridline patterns.

exhibit exact current matching at a set wavelength, and in turn, variance due to discrepancies with nominal layer thickness are not studied numerically. This variability always detracts from performance, and hence is not a means by which one can improve conversion efficiency. In practice, and as shown in the modelled results of figure 8 for example, the efficiency increases with input powers, as long as the beam size and the gridline design is appropriate for the geometry of the device.

2. Tailoring the output voltage of photovoltaic heterostructures

The ability to tailor the device output voltage for various applications is a key feature of the VEHS design. For example, microelectronic applications are likely to require voltages in the 5 V range, while automotive applications are typically more in the 12 V range. Other applications such as biomedical, utilities, telecom, etc may result in demand for intermediate voltages or higher voltage yet, 24 V for instance.

2.1. Design considerations

Tailoring the output voltage of a VEHS device is readily accomplished by adjusting the number N of p/n junctions (PTN), with each individual subcell contributing roughly 1.1–1.2 V. This linear trend in V_{oc} is captured by the experimental data in figure 9, where notably, high efficiencies exceeding 60% are obtained for all of the device configurations studied.

A number of design considerations are apparent from these results. Record efficiencies have been obtained experimentally with up to 20 p/n junctions, and clearly, tailoring the device output voltage to higher values is not too constraining. As elaborated in [8], it is expected that in future work, PT60 devices could readily be implemented, and up to PT100

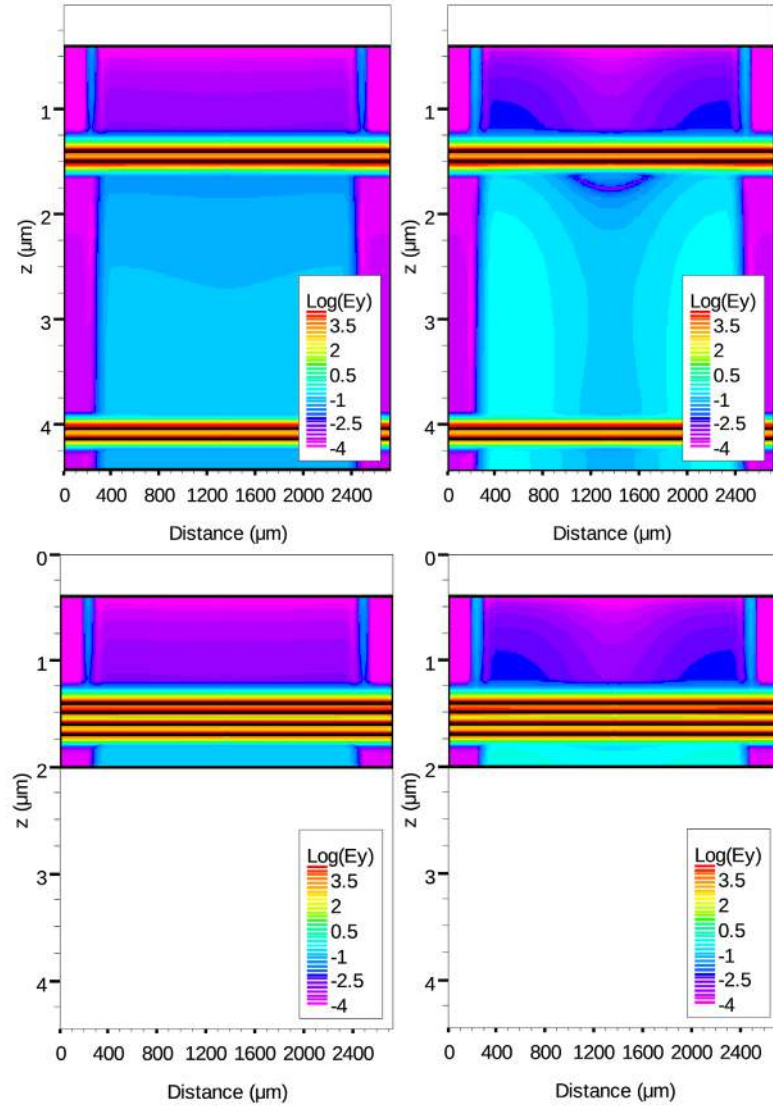


Figure 6. Electric field intensity (logarithm of the vertical component viz $\log(E_y \text{ V}^{-1} \text{ cm})$) for single junction devices with total GaAs thickness 2636 nm (top) and 192 nm (bottom). For each row the device on the left exhibits a high (>80%) fill factor whereas on the right we observe a void in E -field strength characteristic of a low fill factor. Reproduced with permission from [10].

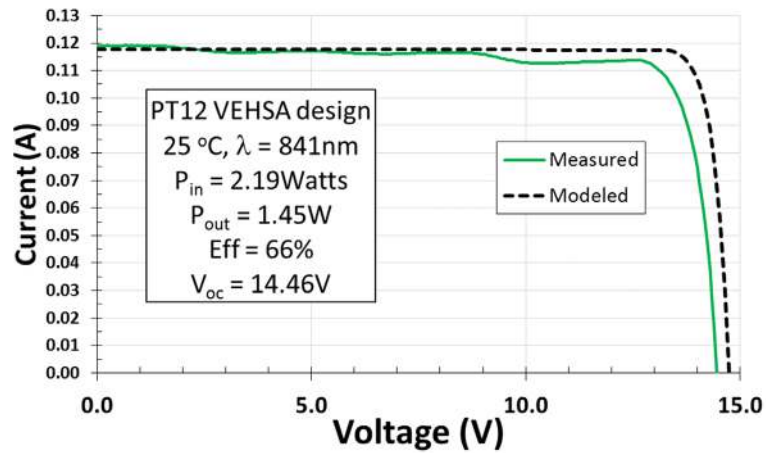


Figure 7. $I(V)$ curve for a PT12 device (modelled curve has $V_{oc} = 14.8 \text{ V}$, $FF = 90.6$ and $Eff = 72.3\%$). © 2016 IEEE. Reprinted, with permission, from [12].

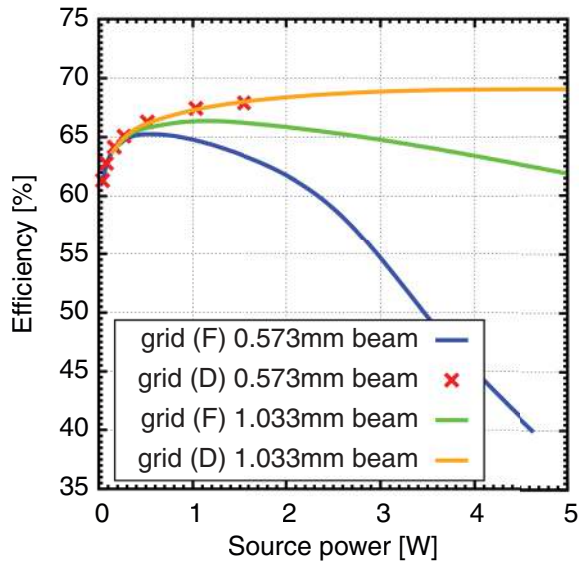


Figure 8. Performance of D and F gridline patterns with increasing source intensity (shown for PT5) with narrow and wide beam profiles. In this graph the D patterned devices are unaffected, whereas the F patterned devices show diminished fill factor, exacerbated at high intensities.

should be also possible by adjusting the design for the energy quantization shifts of the absorption in the thin layers. It has also been demonstrated experimentally that these devices work with high conversion efficiencies at high input powers. Everything else being equal, it is therefore advantageous to operate VEHSAs designed for higher output voltages to minimize the resistive losses, as current scales as $1/N$ and therefore I^2R losses are minimized (especially for high input powers.) Furthermore, as can be seen from the insert of figure 9, high device performance is confirmed for all PTN variants despite significant illumination non-uniformity [7], consistent with our models. However, in applications for which higher output voltages are not required or advantageous, the $N \sim 5\text{--}10$ range tends to yield slightly higher efficiencies in practice due to the increased likelihood of producing an optimal design in fabrication. With these considerations and recalling from the previous sections that higher input intensities are favourable for increasing performance (e.g. via higher voltages), it should be expected that the main requirements for further increasing the record conversion efficiencies in VEHSAs will include:

- (i) working with about 5 p/n junctions,
- (ii) using tunnel junctions with high peak-currents to avoid tunnel junction breakdowns [7],
- (iii) operating at high input intensities to maximize the output voltage,
- (iv) operating the device with efficient heat management to keep the device cool under these conditions.

It should be noted also that the latter conditions have been demonstrated to favour efficient photon recycling effects, in turn helping to correct any residual current mismatch in the VEHSAs structure [45].

Previous sections have already covered device modelling for various structure configurations between PT5 and PT20. With this, a recent study also explored the expected performance for VEHSAs structures up to PT100 [8]. From this modelling, the voltage per p/n junction is expected to remain at $V_{oc} > 1.15$ V for an input power of about 1.4 W. However, as discussed in section 2.1, for a higher number of junctions the current density is proportionally lower. It would therefore be beneficial to operate the VEHSAs structures with high N at higher power or intensities, and therefore further increase the V_{oc} under such conditions. The modelling also shows that the quantization shift can readily be compensated by adding a small percentage of indium to the base/emitter region of the thin p/n junctions as shown in figure 10.

2.2. Exploring the conversion efficiency limits of the VEHSAs heterostructures

Experimental studies on VEHSAs devices published recently [8] have demonstrated:

- (i) the highest photovoltage ever reported for monolithic photovoltaic semiconductor heterostructures with measured open circuit photovoltages of $V_{oc} > 23$ V,
- (ii) the thinnest p/n junctions ever implemented successfully with high-performance in photovoltaic devices, with ultra-thin GaAs bases as small as 24 nm,
- (iii) the highest output powers ever reported for such monolithic PV cells with over 3 W of converted outputs,
- (iv) the highest efficiencies ever reported for any types of optical to electrical power conversion devices simultaneously combining such high photovoltage and high output powers (>3 W at >23 V with $>60\%$ efficiency).

For example, figure 11 demonstrated greater than 3 W of electrical output converted with over 60% efficiencies for the PT12 and the PT20 structures.

As with any photovoltaic device, the optimal conversion efficiency of a VEHSAs is achieved when the product $I_{sc} \times V_{oc} \times FF$ is maximized. The FF value of the PT12 result in figure 11 is essentially maximized at $FF \sim 89\%$, though, we can verify the impact on the efficiency of improvements to V_{oc} and I_{sc} . First, considering I_{sc} , optimal current and minimal thermalization losses are obtained at longer wavelengths near the bandgap. For example, at a wavelength of 850 nm the responsivity is given by $EQE \times \lambda/hc = 0.644 \text{ A W}^{-1}$ for an EQE value of 94%. The EQE can be further augmented by minimizing the reflectivity (improved antireflection coatings) and shadow losses from the gridlines (currently 2%), and by making sure that the current-matching of the VEHSAs structure is well tuned. Therefore, assuming an EQE value of 98% and a longer wavelength of 865 nm, the responsivity would then become 0.684 A W^{-1} . I_{sc} is directly proportional to the responsivity; for the example above, this represents a relative gain of 6%. The PT12 of figure 11 would yield a conversion efficiency of 68.5% for the same V_{oc} of 13.96 V and a FF of 88.9%, but with an improved EQE of 98% at a wavelength of 865 nm. Now considering further V_{oc} improvements,

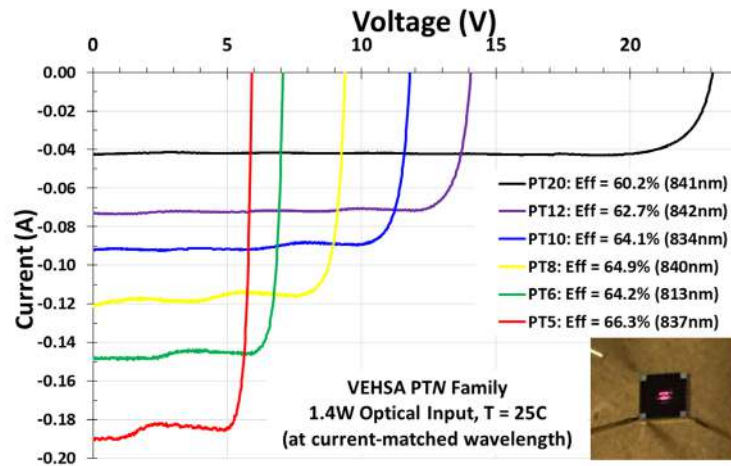


Figure 9. Measured $I(V)$ curves obtained with vertical epitaxial heterostructure architecture (VEHSA) devices prepared with up to $N = 20$ p/n junctions. Reproduced from [8]. CC BY 4.0.

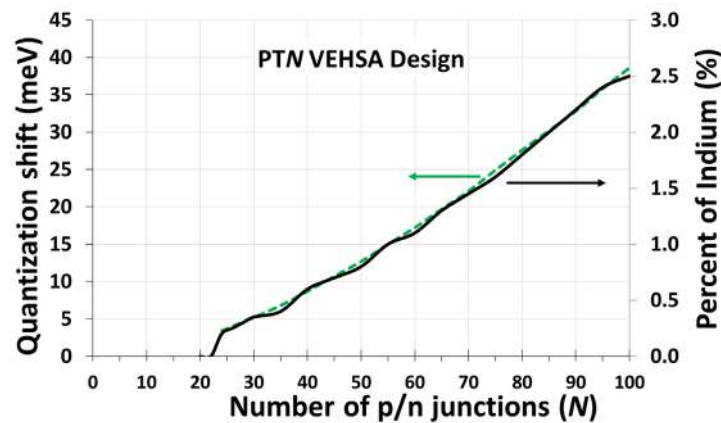


Figure 10. Calculated quantization shift and required indium composition to offset that shift in the thin GaAs/InGaP p/n junctions. Reproduced from [8]. CC BY 4.0.

experimentally V_{oc} values of up to 14.67 V have already been measured. Therefore the PT12 of figure 11 would now have an $\text{Eff} \sim 71.8\%$ for a $V_{oc} \sim 14.67$ V, an FF of 89.0% and an EQE of 98% at a wavelength of 865 nm. Efficiencies would be further improved at higher intensities as V_{oc} increases.

3. Spectral response of the VEHSA devices

3.1. Reaching optimal efficiency

Obtaining the highest possible conversion efficiency for a PTN device involves seeking an optimum among numerous parameters, two of which are total GaAs thickness and source wavelength. The compromise is as follows: at short wavelengths (relative to the band edge) photons are efficiently absorbed, and in turn it is possible to achieve a QE approaching 100% with a relatively thin device. See figure 12: at 830 nm ($\alpha = 12\,837\text{ cm}^{-1}$), evaluating $(1 - e^{-\alpha t})$ yields 99.8% absorption with $t = 5\text{ }\mu\text{m}$ total GaAs thickness (irrespective of the number of subcells). However, the flip side of elevated absorption is that the energy of each photon is in excess of the band gap, thus the overall efficiency is limited by thermalization losses.

Figure 13 complements figure 12 by displaying modelled PV efficiencies as a function of source wavelength at fixed device thickness. In all cases, we note a peak close to 850 nm. With increasing thickness, the marginal gains in efficiency are greatest for the $\alpha = 7414\text{ cm}^{-1}$ graph (i.e. an 860 nm source) therefore this peak would shift to longer wavelength with increasing GaAs thickness, and vice versa. It is interesting to note that from a theoretical standpoint, the optimal configuration is not one tuned to exactly the band edge, but rather a macroscopically thick device tuned to a wavelength slightly below the band edge. In this regime, only phonon mediated transitions into the conduction band are energetically allowed, thus such a device would exhibit thermalization gains (in principle). GaAs VEHSA structures grown with 6 or 7 μm of absorbing lattice-matched semiconductors are not be problematic, therefore VEHSA designs for wavelengths near 860 nm (or slightly longer) are optimal with respect to the above.

Figure 14 illustrates the (incorrectly) modelled impact of detuning on PT12 and PT5 devices—that is, the *would-be* reduction in performance in the absence of photon recycling. These graphs depict a significant reduction in performance with merely 10 nm detuning, a reduction which is not

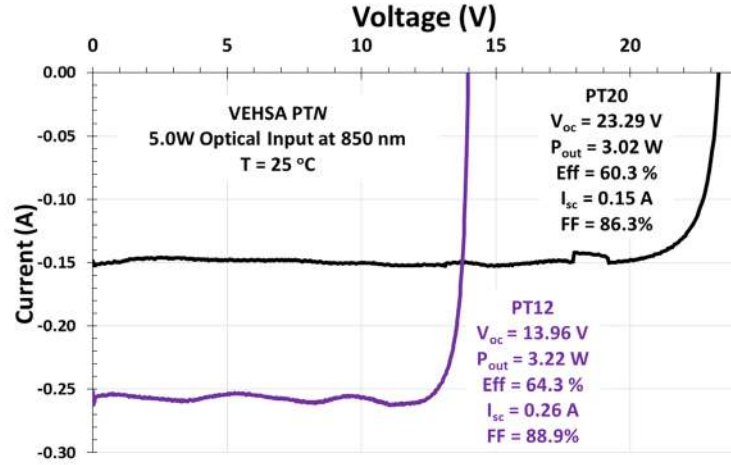


Figure 11. Measured $I(V)$ curves obtained with representative PT12 and PT20 VEHSA devices illuminated with an optical input power of $P_{in} = 5.0$ W. Reproduced from [8]. CC BY 4.0.

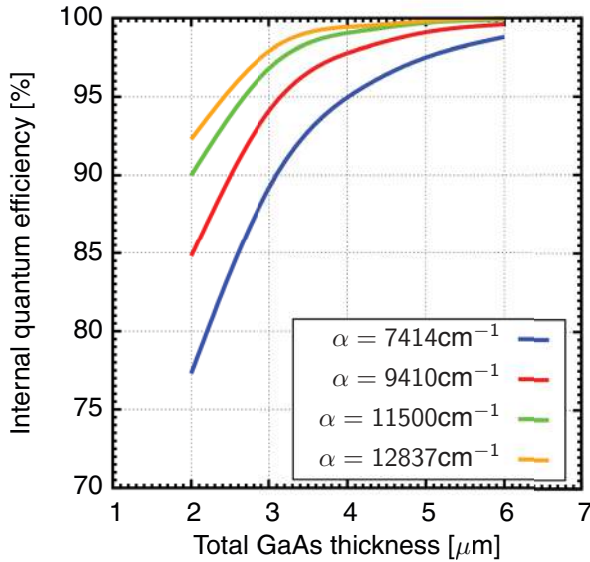


Figure 12. Dependence of quantum efficiency on source wavelength and GaAs thickness.

observed experimentally. In a physical device at high optical input intensities, photon recycling effects are in fact very important in current mismatched conditions [45]. In [45] we have shown that the optimal responsivity of VEHSA devices detuned by 10 nm or more can be nearly fully recovered at higher input intensities, so the result in figure 14 though noteworthy, is misleading.

3.2. PTN with large N

The PT20 device with QE displayed in figure 15 has a base thickness of 24 nm in the topmost (narrowed) subcell. Ignoring quantum effects, the total thickness (t) of this junction approaches

$$t = \frac{1}{\alpha N}. \quad (2)$$

For PT100 (at 850 nm, $\alpha = 9410 \text{ cm}^{-1}$), this would result in a topmost cell thickness of 10 nm.

The $1/N$ dependence in this expression suggests a limit in the largest achievable N , as junctions cannot be grown asymptotically thin. Except, as we approach the thin limit, quantum effects increase the band gap of the junction as it more closely resembles a 2D quantum well (with an increase in band gap of roughly $\sim \hbar^2/mt$ for a junction of thickness t). In effect, at large N the absorption coefficient of the topmost layer diminishes, such that a pure $1/N$ scaling in t would not be realized.

When designing a PTN device in the large N limit, there are a number of factors we must consider when computing the layer thicknesses required for a nominally current-matched heterostructure. Foremost, we must account for diminishing α in the thin limit, which presents a difficulty as α can not be determined analytically. Alternatively, we can adopt a design insisting on a substantially uniform α throughout, achieved by adjusting the Indium content of the thin junctions, as mentioned in the previous section.

The presence of Indium (with molar fractions a few %) can be tuned to counteract the upward shift in bandgap. As a rough calculation, with conduction and valence band offsets of 198 meV and 285 meV respectively, the increase in bandgap for the 10 nm topmost layer in a PT100 device is roughly 39 meV. In turn, such a shift can be compensated by adding a 2.5% Indium fraction to the subcell GaAs. It is worth noting that the addition of Indium introduces compressive strain in the subcell (despite the overall reduction in band gap), and a thorough calculation of the optimal Indium fraction should account for this. Nevertheless, with careful tuning of layer thicknesses, Indium content and induced strain we believe that the design of PTN devices with very large N is practical and achievable.

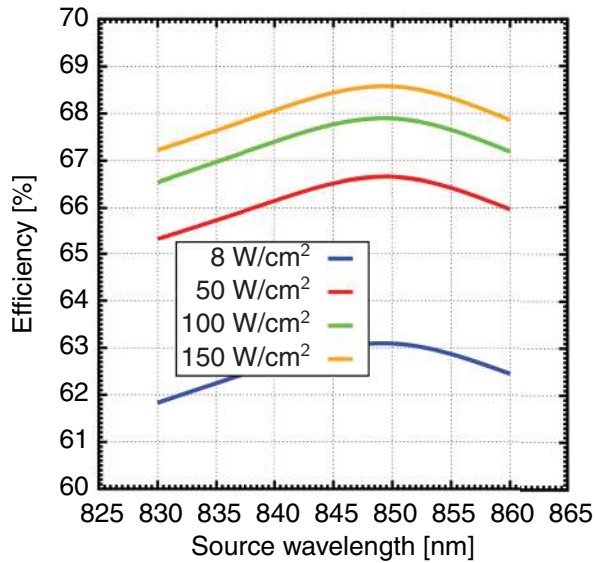


Figure 13. Conversion efficiency of model PT12 devices at varying source intensity tuned to wavelengths in the range 830–860 nm (current matched over the whole axis).

Specifically, e.g. in the case of a PT100 design that would incorporate a top junction of about 10 nm of InGaAs with an indium alloy composition of about 2.5%, the tunnel junction layers could easily incorporate about the same thickness of InGaP with an indium alloy composition lower than the lattice-match point (for example $\sim 2.5\%$ less indium). Because the layers are thin, compressive strain from the junction would then be compensated by tensile strain in the cladding tunnel junction layers.

Achieving VEHSAs with a higher number of p/n junction is relevant to better understanding the physics of photocarriers in nanoscale p/n junctions, and accessing photovoltaic devices capable of even higher photovoltage outputs. Such thin p/n junctions are expected to be more resilient to defects, higher dopings and radiation. Future developments resulting from PTN devices with larger N values include both higher power capabilities and designs from other material systems targeting different ranges of wavelengths.

4. Optical input power response of the VEHSAs devices

4.1. Experimental results obtained with the VEHSAs heterostructures at various input powers

A summary of measured PV conversion efficiencies for various devices is shown in figure 17 with individual data points overlaid on modelled curves for each of PT5, PT6, PT8 and PT12. This graph is intended to be cross-sectional, in that each data point was obtained under slightly different experimental conditions (varying source wavelength / power) with subtle differences between the design of each device (e.g. current matching at differing wavelengths). The same holds for the curves labelled ‘modelled’ as well; in this case the somewhat

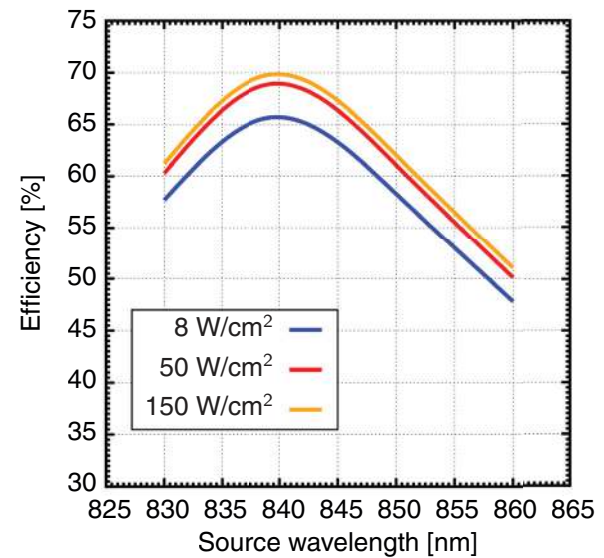
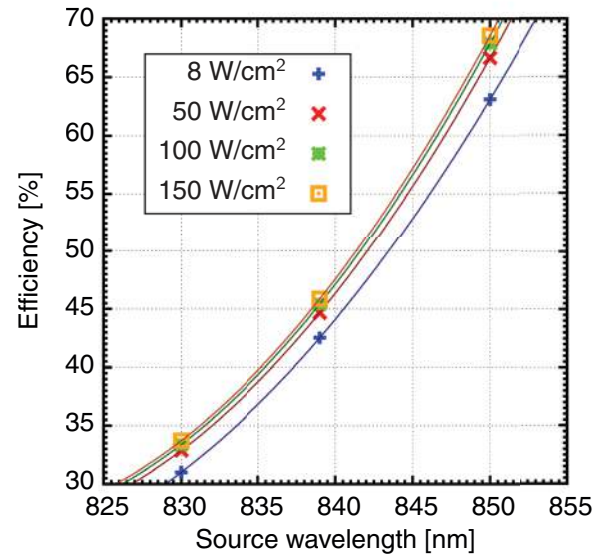


Figure 14. (Upper panel) Conversion efficiency of model PT12 devices at varying source intensities and wavelengths tuned to a design wavelength of 850 nm (current mismatched except at 850 nm). Total GaAs thickness is set at 4200 nm. (Lower panel) Similar content for PT5 (as per the configuration in [6], current-matched at 839 nm), showing both short and long wavelength limits. Reproduced from [6]. CC BY 4.0.

higher efficiency of PT8 relative to PT6 is due to PT8 being tuned to 850 nm with a total GaAs thickness of 4500 nm while PT6 is tuned to 825 nm with total GaAs thickness of 3600 nm. The total absorption of both devices agrees to about 1%; however, the efficiency of PT6 suffers from thermalization losses.

$I(V)$ curves for both PT6 and PT12 are shown in figures 18 and 19 over a range of source intensities. Due to variations in growth, slight current mismatches between adjacent p/n junctions always occurs to some degree, which manifest as undulations in the normally flat part of the $I(V)$ curve. The relative jaggedness of the PT12 graph is indicative of significant detuning; in this regime current mismatches (now

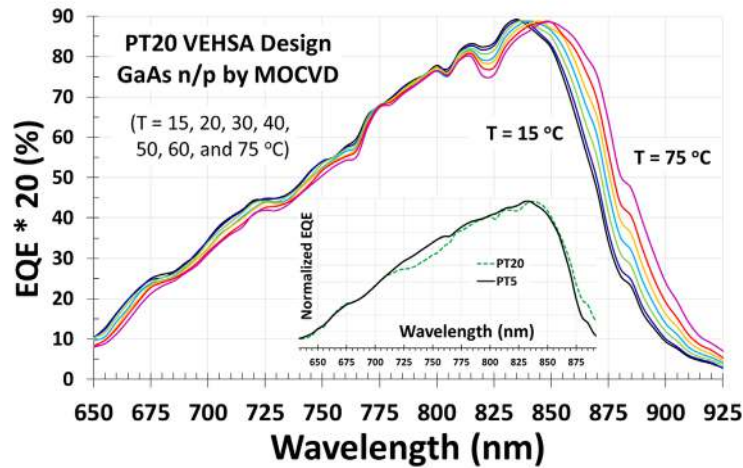


Figure 15. Spectral response of the PT20 device (at various temperatures) contrasted against that of PT5 in the subfigure. Reproduced from [8]. CC BY 4.0.

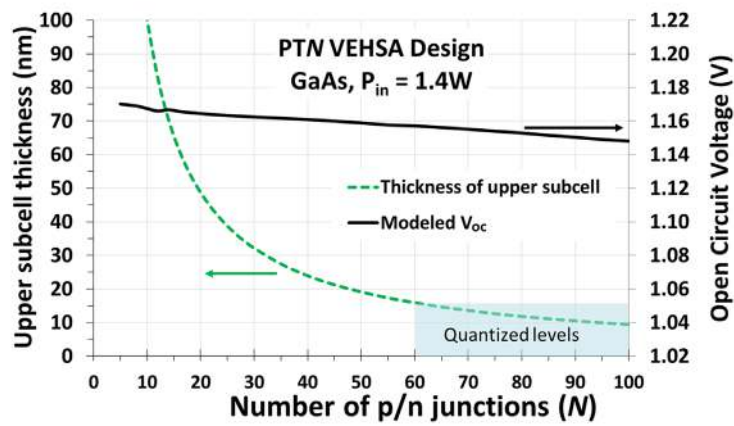


Figure 16. Modelled V_{oc} (not including quantum effects) of the topmost subcell in the thin limit. By excluding quantum effects, the plotted V_{oc} can be interpreted as a lower bound. Reproduced from [8]. CC BY 4.0.

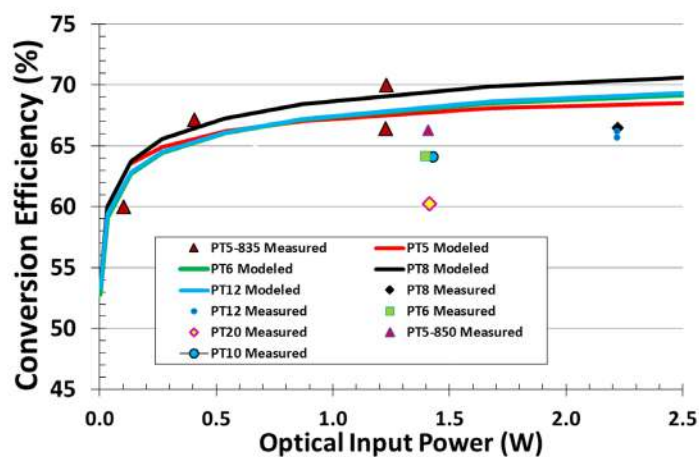


Figure 17. Summary of measured peak conversion efficiencies for various devices, overlaid on modelled data. Adapted from [6, 12]. CC BY 4.0.

exacerbated) cause reverse biases to appear in some of the junctions, which are overcome with increasing applied voltage. Further increases in source intensity could result in

the tunnel junctions becoming resistive—though not shown, the qualitative appearance of the $I(V)$ curve would be similar to the graph for PT12, except with a reduced fill factor.

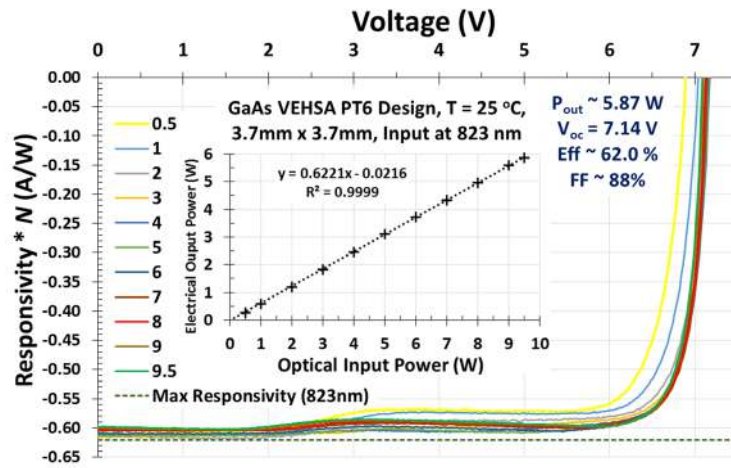


Figure 18. $I(V)$ curve for PT6 current matched at 815 nm with optical input at 823 nm (minor detuning.) [45] John Wiley & Sons© 2016 WILEY-VCH Verlag GmbH & Co. KGaA, Weinheim.

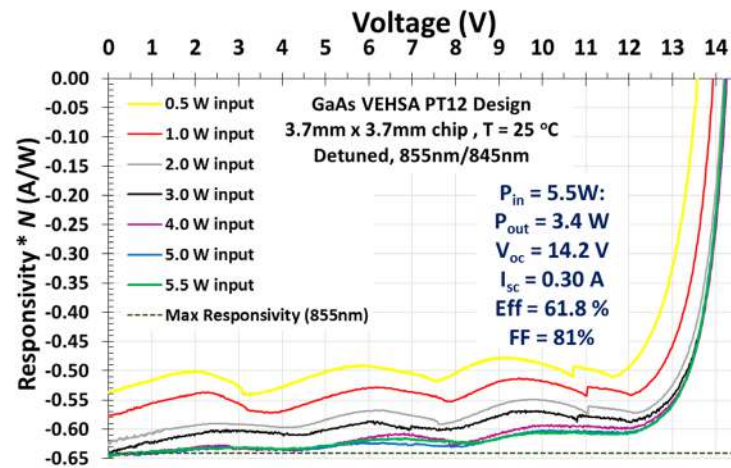


Figure 19. $I(V)$ curve for PT12 current matched at 845 nm with optical input at 855 nm (significant detuning). [45] John Wiley & Sons© 2016 WILEY-VCH Verlag GmbH & Co. KGaA, Weinheim.

In figure 18, an efficiency of 62.0% is obtained for a record-high output power of 5.87 W, obtained by illuminating about 80% of the aperture of a small chip 3.7 mm \times 3.7 mm in area. The device was excited near its optimal wavelength and near optimal responsivity is obtained for most of the input intensities used except for the lowest input powers, in which case the responsivity is slightly diminished. To contrast, in figure 19 the VEHSAs structure is excited at a detuned wavelength. At low power the current mismatch forces the responsivity to decrease significantly to 0.5 A W⁻¹ because of the detuning and the limited current production of under-illuminated subcells. However, the responsivity is remarkably near-fully recovered at higher excitation powers, providing an experimental signature of the strong photon recycling effects in the VEHSAs structures when operated away from their design wavelengths.

A detailed comparison of PT6 and PT12 devices, as shown in figures 17–19 above, helps to provide insight on the evolution of the performance of a PTN with increasing N . $I(V)$ dependence on N was also studied in figures 3, 9 and 11 above, and will be further discussed from the perspective of spectral

response in the next section. For the VEHSAs structures with larger N , current matching would necessitate thinner junctions. These are advantageous to photocarrier extraction and therefore ultimately higher performance is potentially achievable as N increases. Furthermore, as N increases so does output photovoltage while device current decreases proportionally, therefore any performance degradation from resistive losses (I^2R) are consequently minimized. The latter is also advantageous for PTN with larger N , especially for operation at high input powers. However, for a given degree of thickness variations (for example during growth), it should be expected that higher N devices will be more negatively impacted since their junctions are thinner and the relative variation is therefore larger. In practice, the most common variation during epitaxy is an imprecision in the growth rate (e.g. inaccurate calibration) leading to a systematic shift with all junctions being slightly thicker or thinner than intended. The effect of such a systematic shift in thickness simply yields an effective detuning from the nominal peak response. But, as shown for instance in figure 19, performance degradation with detuning is significantly alleviated due to photon coupling effects at high optical

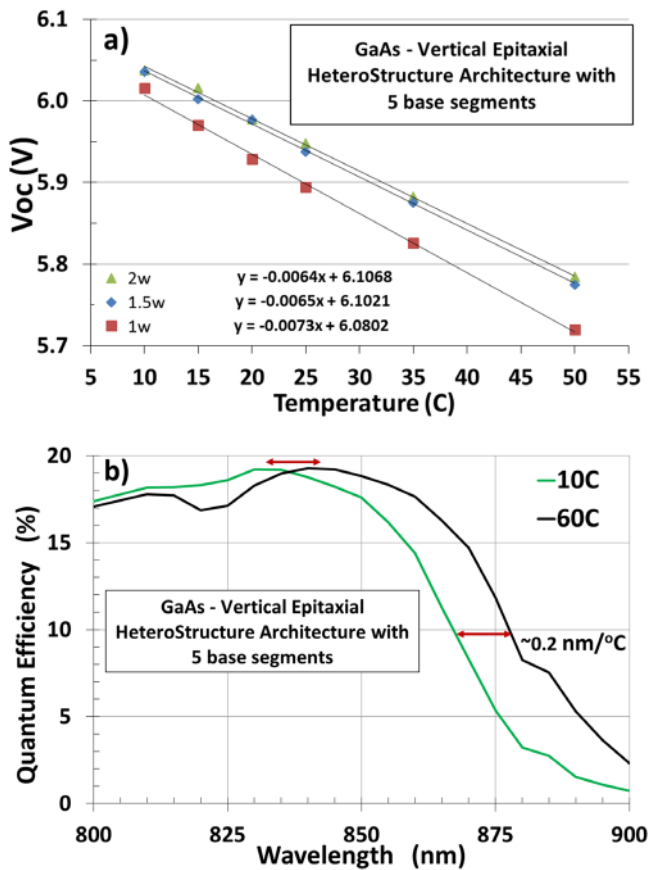


Figure 20. Temperature dependence measured on a monolithic GaAs phototransducer with 5 thin based segments together having a total thickness of $3.5 \mu\text{m}$. V_{oc} is shown in the upper panel for optical input powers of 1.0 W, 1.5 W, and 2.0 W, at a wavelength of 830 nm. A linear regression is fitted to the data to extract dV_{oc}/dT for each input powers. QE is shown in the lower panel for 10 °C and 60 °C. [7] John Wiley & Sons. © 2015 John Wiley & Sons, Ltd.

intensities. Therefore, while random thickness variations can affect VEHSAs with larger N more systematically, experimental results demonstrate that the effect is quite small for the typical level of thickness control obtained with modern epitaxy reactors.

5. Experimental results for VEHSAs device parameters

The PECs are optoelectronic devices that will have to work in various operating environments. It is therefore necessary to study the device behaviour under various conditions and to characterize the evolution of key parameters.

5.1. Temperature effects and PTN coefficients

Typically optoelectronic devices are required to work with a threshold performance over a set temperature range. To extract the temperature coefficients, the performance of the GaAs phototransducers based on a PT5 design was measured at different temperatures and for various input powers [7]. Figure 20 shows the V_{oc} results between 10 °C and 50 °C for the optical input

powers of 1.0 W, 1.5 W, and 2.0 W. The optical input power was obtained from a laser diode emitting at 830 nm. The V_{oc} reduction with temperature can be determined from the slopes in figure 20 (upper panel). It can be observed that it also varies slightly with the incident optical power. A $dV_{oc}/dT = -7.3 \text{ mV } ^\circ\text{C}^{-1}$ is obtained for 1 W input. The dV_{oc}/dT is reduced to $-6.4 \text{ mV } ^\circ\text{C}^{-1}$ for 2 W optical input power.

It has been shown that the values above are consistent with the values obtained with concentrator solar cell such as triple-junction CPV cells. For example, with GaAs, the bandgap variation dE_g/dT is $-0.45 \text{ meV } ^\circ\text{C}^{-1}$, and $dV_{oc}/dT \sim -2.2 \text{ mV } ^\circ\text{C}^{-1}$ has been measured for GaAs solar cells around 1 sun concentration, i.e. for $\sim 0.1 \text{ W cm}^{-2}$. Typically, CPV triple-junction cells have roughly 3 times the temperature dependence with dV_{oc}/dT between -6 and $-7 \text{ mV } ^\circ\text{C}^{-1}$ at 1 sun [34]. The temperature dependence of CPV cells is also reduced with concentration, decreasing to a dV_{oc}/dT of $\sim -4 \text{ mV } ^\circ\text{C}^{-1}$ at 1000 suns ($\sim 100 \text{ W cm}^{-2}$) [7]. It was therefore shown that the temperature behaviour observed in figure 20 (upper panel) is in quantitative agreement with the existing multijunction CPV solar cell data. The temperature coefficients of VEHSAs devices and triple junction (3J) devices can therefore be compared directly with the solar PV results by simply rescaling the measured results by the number of p/n junctions incorporated in the heterostructure. For example, the observed $dV_{oc}/dT \sim -7.3 \text{ mV } ^\circ\text{C}^{-1}$ for the phototransducer with 5 base segments would correspond, after rescaling by a 3/5 factor, to a dV_{oc}/dT of $-4.4 \text{ mV } ^\circ\text{C}^{-1}$ for a triple junction CPV solar cell. The optical density on the phototransducer at 1 W on an area of 3.4 mm^2 corresponds to approximately 29 W cm^{-2} . The PT5 phototransducer exhibits temperature behaviour consistent with a multijunction CPV solar cell.

The temperature shift of the spectral response has also been investigated. Figure 20 (lower panel) shows the external quantum efficiency (EQE) obtained at 10 °C and 60 °C. The QE remains near the optimum value of 100% / 5. It demonstrates that the current balancing in the various base segments is not affected significantly. Indeed, the measurements showed that the peak is shifted by $\sim 0.2 \text{ nm } ^\circ\text{C}^{-1}$ due to the bandgap shift. The QE amplitude however clearly remains near the same value at its peak.

A more detailed study [8] demonstrated that similar temperature behaviours are obtained with the PTN devices for different N , as shown in figure 21. It revealed that EQE values can be used as a valuable gauge for assessing current-matching, and that EQE values can also be used for anticipating the overall photovoltaic conversion efficiencies of the different VEHSAs structures. The behaviour of the EQE peak amplitude with temperature is shown in figure 21 for various numbers of p/n junctions. The results are for representative devices from the complete family of VEHSAs structures. Figure 21 highlights examples when the EQE amplitude increases with temperature in curve (i), or it reaches a peak at intermediate temperatures in curve (ii), or it decreases with temperature in curve (iii). The behaviour is related to the temperature fine-tuning of the absorption of the various junctions relative to original current-mismatching.

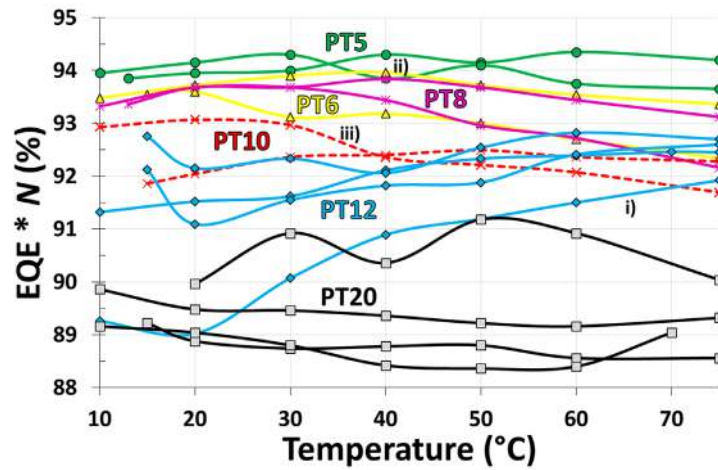


Figure 21. Detailed analysis of the dependence of the EQE peak amplitude on the temperature and on the number (N) of p/n junctions for various PTN devices. Examples are highlighted when the EQE amplitude increases with temperature in curve (i), reaches a peak at intermediate temperatures in curve (ii), or decreases with temperature in curve (iii). A minor trend for lower EQE amplitudes is also noticeable as N increases. Reproduced from [8]. CC BY 4.0.

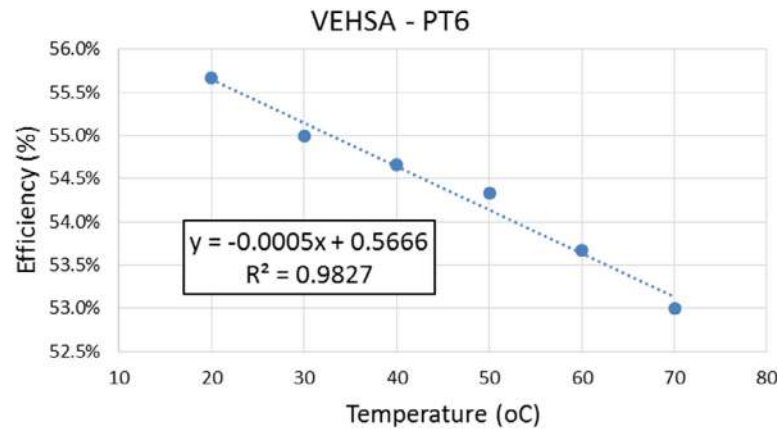


Figure 22. Temperature dependence for a PT6 device measured at 3 W optical input, showing the measured efficiency dependence. Reproduced with permission from [11].

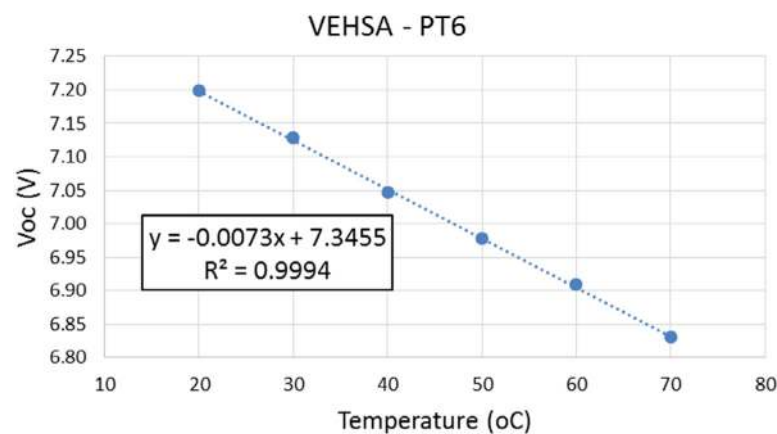


Figure 23. Temperature dependence for a PT6 device measured at 3 W optical input, showing the measured open circuit voltage (V_{oc}) dependence. Reproduced with permission from [11].

As mentioned in the previous sections, a trend for slightly lower EQE amplitudes is also noticeable as N increases. The slight variations in the accuracy of the current-matching with

respect to the optimal design are presumably causing this behaviour. Nominal designs are intended to achieve optimal current-matching between the various subcells at a specific

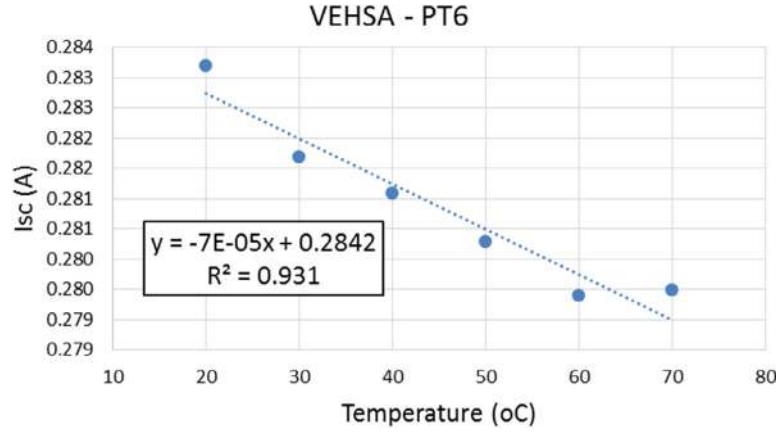


Figure 24. Temperature dependence for a PT6 device measured at 3 W optical input, showing the measured short circuit current (I_{sc}) dependence. Reproduced with permission from [11].

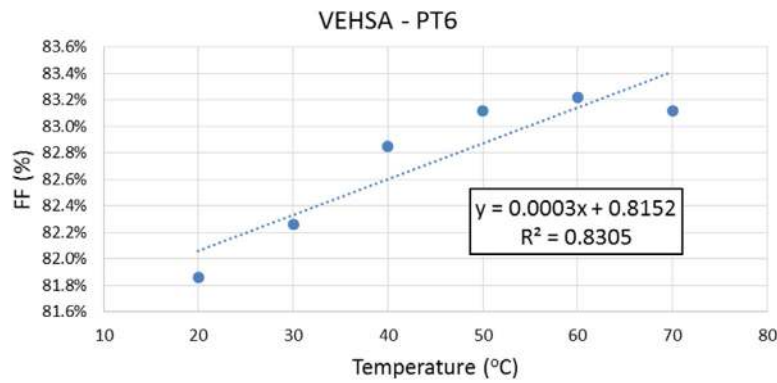


Figure 25. Temperature dependence for a PT6 device measured at 3 W optical input, showing the measured fill-factor (FF) dependence. Reproduced with permission from [11].

wavelength and at a specific temperature. The VEHSA structures offer a good tolerance on wavelength detuning and temperature variations. If the implemented subcell thicknesses are marginally off from an optimal design, a temperature fine-tuning of the absorption coefficient can slightly improve or further deteriorate the current-matching in the stack of subcells as observed in curves (i) and (iii) respectively. A high EQE is detected throughout the temperature range if the current matching was initially accurate. Under those conditions a peak in EQE amplitude can be observed at an intermediate temperature. This is seen in curve (ii) of figure 21 and it was the case for PT5, PT6, or PT8 studied in [8].

For PTN devices with a larger N , temperature dependence increase with the number of p/n junctions. As an example, V_{oc} , short-circuit current (I_{sc}) and fill factor (FF) for the PT6 devices is shown in figures 22–25 (measurements were obtained with 3 W input power, and the optical input was slightly detuned from the peak efficiency.) From figure 22, an efficiency reduction of about $0.05\%(\text{abs})\text{ }^{\circ}\text{C}^{-1}$ is found for the PT6. The V_{oc} reduction at 3 W for the PT6 is about $-7.3\text{ mV }^{\circ}\text{C}^{-1}$ from figure 23. This is a little higher but consistent with the earlier values obtained for the PT5 when considering that 6 p/n junctions were used instead of 5. Using the PT5 data at 2 W and a linear relationship with the number of p/n junctions, a V_{oc} reduction

of $-6.4/5 \times 6 = -7.7\text{ mV }^{\circ}\text{C}^{-1}$ at 2 W was expected for the PT6. The measured $-7.3\text{ mV }^{\circ}\text{C}^{-1}$ is lower because the data was obtained at 3 W instead of 2 W. As discussed above, the V_{oc} reduction decreases with increasing powers. In figure 24, the I_{sc} is relatively flat with temperature but here it decreases with a small slope. Figure 25 shows that the FF increases with temperature. But as mentioned above, the exact behaviour of I_{sc} and FF can depend on the exciting wavelength and its position with respect to the peak response of the PTN device. The temperature coefficients extracted from the measurements can be used to populate the expected values of V_{oc} for different PTN at various temperatures. Figure 26 shows the results for an optical input power of about 3 W.

5.2. Photovoltaic output voltage optimization for thin p/n junctions

The modelling of section 1.5 detailed the parameters affecting the output voltage of the VEHSA devices. Moreover, the use of thin p/n junctions yields augmented V_{oc} values, as illustrated in section 1 by comparing the V_{oc} results of a 6-junction device designed with a planar architecture made of standard p/n junctions, to a PT6 device designed with 6 thin vertical p/n junctions. In this comparison, a gain of $\sim 92\text{ mV}$ per p/n junction was observed with respect to the planar device [45]. Higher

VEHSA design	V_{oc}		
	25 °C	45 °C	105 °C
PT#	(Volts)	(Volts)	(Volts)
2	2.4	2.4	2.2
3	3.7	3.6	3.4
4	4.9	4.8	4.5
5	6.1	6.0	5.6
6	7.3	7.2	6.7
7	8.5	8.4	7.9
8	9.8	9.6	9.0
9	11.0	10.8	10.1
10	12.2	12.0	11.2
11	13.4	13.2	12.3
12	14.6	14.3	13.5
13	15.9	15.5	14.6
14	17.1	16.7	15.7
15	18.3	17.9	16.8
16	19.5	19.1	18.0
17	20.7	20.3	19.1
18	22.0	21.5	20.2
19	23.2	22.7	21.3
20	24.4	23.9	22.5

Figure 26. Expected V_{oc} values for various PTN structures, extrapolated from the measured temperature coefficients at an optical input power of about 3 W.

V_{oc} can also be obtained by operating at higher optical intensities, but only as long as the temperature of the junctions is not increased due to an insufficient thermal management capacity. Output voltages as high as 1.223 V per p/n junctions have been measured with a PT12 device under 4.4 W at 25 °C [10].

5.3. Device response time of VEHSA structures

For some applications, the response time of the VEHSA must be considered. The vertical architecture of the VEHSA device incorporates multiple p/n junction in series, each of the p/n junction having a characteristic capacitance. Therefore the overall capacitance of the PTN device is expected to be a factor of $1/N$ smaller than the capacitance of the individual p/n junctions. A lower capacitance can be advantageous for the time response of the PECs device. For example, Masson did some preliminary LT Spice modelling which revealed that the PT12 can have a rise time of $\sim 0.1 \mu\text{s}$ for a load of 100Ω as shown in figure 27 [53].

5.4. Device tolerance to optical input beam non-uniformity and impact on performance

The VEHSA PEC design resolves the non-uniformity and misalignment problems which often affect planar geometries. The much improved tolerance [7, 12] with respect to source alignment and non-uniformity is illustrated in

figure 28. Similar to the measurements presented in the earlier section where efficiencies greater than 60% were obtained for all the devices of the PTN family (obtained with a non-uniform beam as shown in the insert of figure 9), the measurements in figure 28 are for conditions in which the beam is mostly concentrated within a small fraction of the cell area. Here, the beam is defined via the extent of the acceptance cone of the source emerging from the $300 \mu\text{m}$, $\text{NA} = 0.22$ fibre, and the arrangement is significantly under-filling the active surface. As can be seen, when the beam is approached closer to the cell, efficiency actually increases. Such an increase for a non-uniform beam with higher intensity is compatible with the photon recycling effect for an input beam slightly detuned with respect to the VEHSA device. For these conditions, the effect becomes magnified for an input beam with a higher intensity concentrated on a fraction of the active area of the cell. Thus, the VEHSA devices have been demonstrated to be very robust to non-uniform illumination conditions.

6. Applications

VEHSA PECs have been realized in various configurations with record optical to electrical conversion efficiencies. The unprecedented performance can be obtained with high output photovoltages adapted for various applications. For example, VEHSA phototransducers have been configured into opto-coupler configurations to provide isolated power supply sources with high galvanic isolation capabilities. The following section will therefore present an overview of the opto-coupler results obtained with VEHSA PECs.

6.1. Device benefits for optoelectronic applications

Given the unprecedented performance of the VEHSA PECs, it is interesting to study the performance of opto-coupler (OC) devices built by integrating a high-power laser diode with a PTN device [10, 11]. A laser diode and a PTN device were arranged in a face-to-face configuration, and an air gap of about 1 mm was used to provide high galvanic isolation. The geometry was not optimized for these initial tests; e.g. slightly larger VEHSA chips would be advantageous to avoid cases for which a small fraction of the laser output beam may not have been perfectly matched to the phototransducer active area. The wavelength detuning was small for the PT8 and PT12 devices studied here.

High optical-to-electrical (O-E) and electrical-to-electrical (E-E) efficiencies have been observed, as shown in figure 29. The maximum opto-coupler E-E here is at about 26% for an opto-coupler electrical output between about 1.7 W and 2.6 W. The opto-coupler based on the PT8 phototransducers provides similar performance. High opto-coupler output powers exceeding 3 W were demonstrated in that study.

The PT6 phototransducers used here are tuned at about 820 nm and are therefore detuned for an input at 850 nm. The opto-coupler based on the PT6 phototransducers are therefore

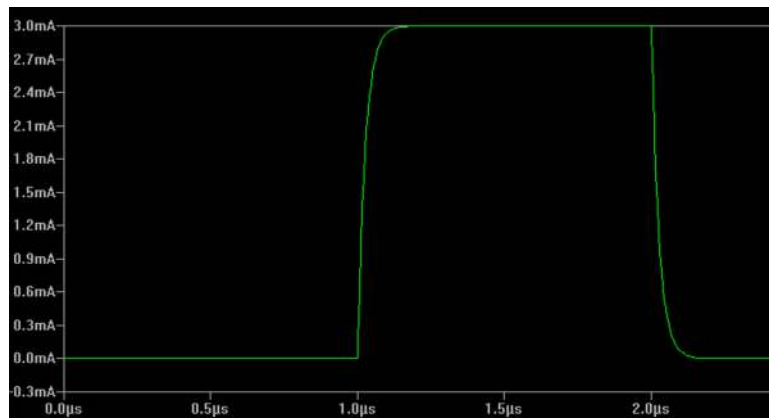


Figure 27. Modelling of PT12 response time based on LT Spice simulation using a 100 Ω load.

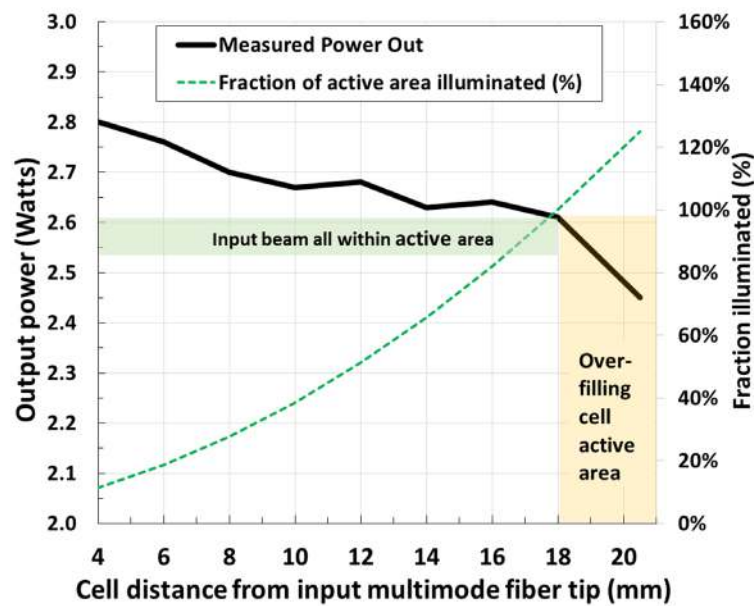


Figure 28. Power output of a 6J device illuminated via a 300 μm core, NA = 0.22 fibre at 825 nm. © 2016 IEEE. Adapted, with permission, from [12].

VEHSA type	Laser Current	Laser Voltage	Laser Output Power	Laser Eff	PT's Voc	PT's Isc	PT's Pmax	PT's O-E Eff	OC's E-E Eff
	A	V	W	%	V	mA	W	%	%
PT12	1.0	1.63	0.15	9.1	13.49	10	0.12		7.3%
PT12	1.5	1.68	0.68	27.1	14.14	33	0.42	61.1%	16.6%
PT12	2.0	1.74	1.22	35.0	14.34	57	0.72	58.9%	20.6%
PT12	2.5	1.80	1.76	39.3	14.47	82	1.04	59.1%	23.2%
PT12	3.0	1.85	2.31	41.6	14.54	109	1.40	60.9%	25.3%
PT12	3.5	1.90	2.84	42.7	14.57	134	1.73	60.8%	26.0%
PT12	4.0	1.95	3.37	43.2	14.62	157	2.03	60.2%	26.0%
PT12	4.5	2.00	3.89	43.2	14.66	180	2.35	60.4%	26.1%
PT12	5.0	2.05	4.41	43.1	14.67	206	2.64	59.8%	25.7%
PT12	5.5	2.10	4.91	42.6	14.65	225	2.91	59.2%	25.2%
PT12	6.0	2.14	5.40	42.1	14.63	247	3.19	59.0%	24.8%
PT8	2.5	1.80	1.76	39.3	9.71	124	1.07	60.9%	23.9%
PT6 (detuned)	2.5	1.80	1.76	39.3	7.24	154	0.95	53.7%	21.1%

Figure 29. Opto-coupler (OC) performance obtained in the face-to-face configuration of an 850 nm laser diode and various PTN phototransducers. Reproduced with permission from [11].

yielding an E–E performance about 10% lower relative to a tuned PTN device.

6.2. Considerations for tailoring the spectral response

VEHSA devices based on the GaAs material system cover well the 750–875 nm spectral range. Additionally, photon coupling effects have been demonstrated to broaden the spectral range for which the VEHSA devices convert high-power optical inputs with high efficiencies into an electrical output having a preset voltage [45]. High optical input intensities are therefore advantageous to maximize the effectiveness of photon recycling effects and therefore preserve a high responsivity over a significantly broader wavelength range. Given that comparable photon recycling effects can be obtained at lower powers by reducing the size of the beam and of the chip, it can therefore be advantageous to consider achieving high optical intensities by reduced dimensions.

Smaller chips operated at reduced powers can also ease the thermal constraints and further improve V_{oc} . The maximum practical intensities are restricted by the limit in current density that the tunnel junctions can handle [7] or by the destruction threshold for the materials deposited on the input surface of the device, including the gridlines and antireflection coatings. We find that for optimized tunnel junction designs, the gridlines are damaged before the tunnel junction peak current is exceeded. Hence, it is practically possible to exploit photon coupling effects to broaden the spectral response of the VEHSA devices.

The implementation of VEHSA devices in other semiconductor materials can also be necessary to reach the additional wavelength ranges required for various applications. For example, the common availability of other optoelectronic devices, such as high-power 980 nm semiconductor laser diodes, or the specific wavelength requirements of some important applications can also dictate the needs for developing novel III–V heterostructures that are adapted to these specific requirements. As with the progress made so far on the GaAs material system, it will be interesting to develop heterostructures that will benefit from the properties of InP, Si, and Ge material systems as examples. InP-based VEHSA heterostructures can be developed to address the 980 nm and the 1300 nm application requirements by using ternary InGaAs and quaternary InGaAsP alloys. The doping profiles would need to be optimized, but the favourable surface recombination velocities in these materials should allow for the successful implementation of VEHSA PECs. For Si and Ge, Si p/n junctions could be grown with SiGe tunnel junctions in a group IV epitaxy system. For Ge-based VEHSA devices, hybrid III–V group IV epitaxy could allow the growth of Ge p/n junctions on Ge substrates with GaAs tunnel junctions.

6.3. Considerations for tailoring the output power

Studies performed with VEHSA devices fabricated in $3.7\text{ mm} \times 3.7\text{ mm}$ chips have demonstrated output powers as high as 5.87 W with a conversion efficiency greater than

60% [45]. The converted output power can readily be further increased by increasing the size of the chip or by combining the output power of several chips.

6.4. Overall trends and future developments in the field

Further developments in the field of VEHSA devices will likely cover:

- optimizing the device design to reach higher conversion efficiencies and higher photovoltages yet,
- integrating the ultra-high efficiency PV devices in subsystems that will take advantage of their unique properties, and
- implementing the VEHSA devices in other semiconductor materials to reach the additional wavelength ranges required for other applications.

7. Summary and conclusions

Optical to electrical power converting semiconductor devices were achieved with breakthrough performance by designing a Vertical Epitaxial HeteroStructure Architecture (VEHSA design). The devices are featuring modelled and measured conversion efficiencies greater than 65%. The ultrahigh conversion efficiencies were obtained by monolithically integrating several thin GaAs photovoltaic junctions tailored with submicron absorption thicknesses and grown in a single crystal by epitaxy. The heterostructures that were engineered with a number N of such ultrathin junctions yielded optimal external quantum efficiencies approaching $100\%/N$ and individual nanoscale junctions each generating about 1.2 V of output voltage (in series) when illuminated in the infrared.

The optoelectronic properties of phototransducers prepared with designs having 5 to 20 junctions have been studied. Record-high photovoltages have been obtained with the VEHSA with 20 thin p/n junctions (PT20). Open circuit photovoltages in excess of 23 V have been measured for a continuous wave monochromatic optical input power of $\sim 1\text{ W}$ tuned in the 750–875 nm wavelength range. Conversion efficiencies greater than 60% have been demonstrated for all devices studied in the PTN family. For the PT20 structure the narrowest ultrathin base was achieved with a thickness of only 24 nm. A detailed analysis has been made for the EQE dependence with temperature and for VEHSA structures realized with a varied number of p/n junctions. Modelling of the photovoltage performance of devices designed with thinner bases has been studied. For example, the narrowest subcell of a PT60 structure would have a base as thin as 8 nm, and it is expected to still generate an individual subcell photovoltage of 1.14 V. Such narrow p/n junctions will begin to feature 2-dimensional quantum well effects and the impact on the absorption can be adjusted by adding indium to the thin p/n junctions.

Photon-recycling effects have been studied in the VEHSA devices. The responsivity of VEHSA structures with multiple

thin GaAs p/n junctions have been measured for various optical input powers and for different wavelength detuning values with respect to the peak of the spectral response. While the detuning of the optical excitation decreases the external quantum efficiency and the responsivity at low input powers, it has been demonstrated that at high optical intensities, a large fraction of the performance can be recovered despite significant detuning values. Photon coupling effects have been demonstrated experimentally to broaden the spectral range for which the VEHSAs devices convert high-power optical inputs with high efficiencies into an electrical output having a preset voltage.

The devices exhibited a near optimum responsivity of up to 0.645 A W^{-1} for tuned excitation conditions or at high optical intensities for spectral detuning values of up to $\sim 25 \text{ nm}$ and corresponding to an external quantum efficiency of $\sim 94\%$. Efficiencies of 62.0% and 61.8% have been obtained for current-matched excitations and for a detuning of $>10 \text{ nm}$ respectively. A record output power of 5.87 W has been reported. An open circuit voltage enhancement of 92 meV per p/n junction has been measured compared to a device with a planar architecture.

In conclusion, the photovoltaic VEHSAs design allows one to achieve a near-optimum responsivity, an improved photovoltage output compared to p/n junctions with standard thicknesses, and low series resistance and shunting effects yielding high fill-factor values. Record optical to electrical conversion efficiency values have been obtained at unprecedented output powers and paths toward even higher performance have been identified.

Acknowledgments

The authors would like to acknowledge our collaborators including the authors of [6–12, 16, 54], as well as all of the sources of funding in those respective papers. We would like to thank in particular D Masson and F Proulx for their significant contributions throughout.

References

- [1] Werthen J G, Widjaja S, Wu T C and Liu J 2005 Power over fiber: a review of replacing copper by fiber in critical applications *Optics & Photonics 2005 (International Society for Optics and Photonics)* (Bellingham, WA: SPIE) p 58710C
- [2] Bett A W, Dimroth F, Lockenhoff R, Oliva E and Schubert J 2008 III–V solar cells under monochromatic illumination *33rd IEEE Photovoltaic Specialists Conf.* (IEEE) pp 1–5
- [3] Reichmuth S K, Helmers H, Philipps S P, Schachtner M, Siefer G and Bett A W 2016 *Prog. Photovolt., Res. Appl.* at press (<https://doi.org/10.1002/pip.2814>)
- [4] Marblestone A H *et al* 2013 Cornell University Library (arXiv:1306.5709)
- [5] de Nazare F V B and Werneck M M 2012 *IEEE Sensors J.* **12** 1193–4
- [6] Fafard S, York M, Proulx F, Valdivia C, Wilkins M, Arès R, Aimez V, Hinzner K and Masson D 2016 *Appl. Phys. Lett.* **108** 071101
- [7] Masson D, Proulx F and Fafard S 2015 *Prog. Photovolt., Res. Appl.* **23** 1687–96
- [8] Fafard S, Proulx F, York M, Richard L, Provost P, Arès R, Aimez V and Masson D 2016 *Appl. Phys. Lett.* **109** 131107
- [9] York M, Proulx F, Masson D P, Jaouad A, Bouzazi B, Arès R, Aimez V and Fafard S 2016 *MRS Adv.* **1** 881–90
- [10] York M C, Proulx F, Masson D P, Jaouad A, Bouzazi B, Arès R, Aimez V and Fafard S 2016 Enhanced photocarrier extraction mechanisms in ultra-thin photovoltaic GaAs n/p junctions *SPIE OPTO (International Society for Optics and Photonics)* (Bellingham, WA: SPIE) p 97430Y
- [11] Fafard S *et al* 2016 Advances with vertical epitaxial heterostructure architecture (vehsa) phototransducers for optical to electrical power conversion efficiencies exceeding 50 percent *SPIE OPTO (International Society for Optics and Photonics)* (Bellingham, WA: SPIE) p 97430Y
- [12] Fafard S *et al* 2016 Ultra-efficient n-junction photovoltaic cells with $V_{oc} > 14 \text{ V}$ at high optical input powers *IEEE 43rd Photovoltaic Specialists Conf.* (IEEE) pp 2374–8
- [13] King R, Law D, Edmondson K, Fetzer C, Kinsey G, Yoon H, Sherif R and Karam N 2007 *Appl. Phys. Lett.* **90** 183516–900
- [14] Green M A, Emery K, Hishikawa Y, Warta W and Dunlop E D 2015 *Prog. Photovolt., Res. Appl.* **23**
- [15] Wilkins M, Valdivia C E, Gabr A M, Masson D, Fafard S and Hinzner K 2015 *J. Appl. Phys.* **118** 143102
- [16] Wilkins M, Valdivia C E, Chahal S, Ishigaki M, Masson D P, Fafard S and Hinzner K 2016 *SPIE OPTO (International Society for Optics and Photonics)* (Bellingham, WA: SPIE) p 97430W
- [17] Cui Y, van Dam D, Mann S A, van Hoof N J, van Veldhoven P, Garnett E C, Bakkers E P and Haverkort J E 2016 *Nano Lett.* **16** 6467–71
- [18] Khvostikov V, Kalyuzhnyy N, Mintairov S, Sorokina S, Potapovich N, Emelyanov V, Timoshina N K and Andreev V 2016 *Semiconductors* **50** 1220–4
- [19] Steiner M, Geisz J, Garcia I, Friedman D, Duda A and Kurtz S 2013 *J. Appl. Phys.* **113** 123109
- [20] Miller O D, Yablonovitch E and Kurtz S R 2012 *IEEE J. Photovolt.* **2** 303–11
- [21] Behaghel B *et al* 2015 *Appl. Phys. Lett.* **106** 081107
- [22] Vandamme N, Chen H L, Gaucher A, Behaghel B, Lemaitre A, Cattoni A, Dupuis C, Bardou N, Guillemoles J F and Collin S 2015 *IEEE J. Photovolt.* **5** 565–70
- [23] Rau U, Paetzold U W and Kirchartz T 2014 *Phys. Rev. B* **90** 035211
- [24] Liang D, Kang Y, Huo Y, Chen Y, Cui Y and Harris J S 2013 *Nano Lett.* **13** 4850–6
- [25] Kang K, Xie S, Huang L, Han Y, Huang P Y, Mak K F, Kim C J, Muller D and Park J 2015 *Nature* **520** 656–60
- [26] Lee S M, Kwong A, Jung D, Faucher J, Shen L, Biswas R, Lee M L and Yoon J 2015 *ACS Nano* **9** 10356–65
- [27] Sweet C A, Schulte K L, Simon J D, Steiner M A, Jain N, Young D L, Ptak A J and Packard C E 2016 *Appl. Phys. Lett.* **108** 011906
- [28] Kim J, Hwang J, Song K, Kim N, Shin J C and Lee J 2016 *Appl. Phys. Lett.* **108** 253101
- [29] LeVan P D, Sood A K, Wijewarnasuriya P and D'Souza A I 2014 Infrared sensors, devices, and applications *Proc. SPIE* **9220** 922001
- [30] Collin S, Vandamme N, Goffard J, Cattoni A, Lemaitre A and Guillemoles J F 2015 Ultrathin GaAs solar cells with a nanostructured back mirror *IEEE 42nd Photovoltaic Specialist Conf.* (IEEE) pp 1–3
- [31] Aeberhard U 2016 *Appl. Phys. Lett.* **109** 033906
- [32] Hirst L, Yakes M, Warner J, Bennett M, Schmieder K, Walters R and Jenkins P 2016 *Appl. Phys. Lett.* **109** 033908
- [33] Kabi S, Das T and Biswas D 2010 *Phys. E: Low-Dimens. Syst. Nanostruct.* **42** 2131–3

- [34] Höhn O, Walker A, Bett A and Helmers H 2016 *Appl. Phys. Lett.* **108** 241104
- [35] Oliva E, Dimroth F and Bett A 2008 *Prog. Photovolt., Res. Appl.* **16** 289–915
- [36] Andreev V, Khvostikov V, Kalinovsky V, Lantratov V, Grilikhes V, Rumyantsev V, Shvarts M, Fokanov V and Pavlov A 2003 High current density gaas and gasb photovoltaic cells for laser power beaming *Proc. of 3rd World Conf. on Photovoltaic Energy Conversion* vol 1 (IEEE) pp 761–4
- [37] Lumb M P, Steiner M A, Geisz J F and Walters R J 2014 *J. Appl. Phys.* **116** 194504
- [38] Walker A, Höhn O, Micha D, Wagner L, Helmers H, Bett A and Dimroth F 2015 Impact of photon recycling and luminescence coupling in III–V photovoltaic devices *SPIE OPTO (International Society for Optics and Photonics)* (Bellingham, WA: SPIE) p 93580A
- [39] Schubert J, Oliva E, Dimroth F, Guter W, Loeckenhoff R and Bett A 2009 *IEEE Trans. Electron Dev.* **56** 170–5
- [40] Walker A, Heckelmann S, Karcher C, Höhn O, Went C, Niemeyer M, Bett A and Lackner D 2016 *J. Appl. Phys.* **119** 155702
- [41] Steiner M A *et al* 2016 *IEEE J. Photovolt.* **6** 358–65
- [42] Eyderman S and John S 2016 *Sci. Rep.* **6** 28303
- [43] Mohammad S, Chowdhury I U I, Islam S and Bhuiyan A G 2015 Effects of photon recycling on the properties of p + n gaas solar cell *2nd Int. Conf. on Electrical Information and Communication Technology* (IEEE) pp 456–60
- [44] Walker A W, Höhn O, Micha D N, Bläsi B, Bett A W and Dimroth F 2015 *IEEE J. Photovolt.* **5** 1636–45
- [45] Proulx F, York M, Provost P, Arès R, Aimez V, Masson D and Fafard S 2017 *Phys. Status Solidi RRL* **11** 1600385
- [46] Ahrenkiel R, Keyes B and Dunlavy D 1991 *J. Appl. Phys.* **70** 225–31
- [47] Lush G, MacMillan H, Keyes B, Levi D, Melloch M, Ahrenkiel R and Lundstrom M 1992 *J. Appl. Phys.* **72** 1436–42
- [48] Johnson S, Ding D, Wang J B, Yu S Q and Zhang Y H 2007 *J. Vac. Sci. Technol. B* **25** 1077–82
- [49] Sotoodeh M, Khalid A and Rezazadeh A 2000 *J. Appl. Phys.* **87** 2890–900
- [50] Leite M S, Woo R L, Munday J N, Hong W D, Mesropian S, Law D C and Atwater H A 2013 *Appl. Phys. Lett.* **102** 033901
- [51] Luo H, Shen W, Zhang Y and Yang H 2002 *Phys. B: Condens. Matter* **324** 379–86
- [52] Jain S and Roulston D 1991 *Solid-State Electron.* **34** 453–65
- [53] Masson D 2016 unpublished
- [54] Valdivia C E, Wilkins M M, Bouzazi B, Jaouad A, Aimez V, Arès R, Masson D P, Fafard S and Hinzer K 2015 Five-volt vertically-stacked, single-cell gaas photonic power converter *SPIE OPTO (International Society for Optics and Photonics)* (Bellingham, WA: SPIE) p 93580E